RESEARCH PAPER



Paved guideway topology optimization for pedestrian traffic under Nash equilibrium

Xiaojia Shelly Zhang^{1,2} • Weichen Li¹ • Yanfeng Ouyang¹

Received: 21 February 2020 / Revised: 24 August 2020 / Accepted: 19 October 2020 / Published online: 16 January 2021 © Springer-Verlag GmbH Germany, part of Springer Nature 2021

Abstract

Without proper flow channelization, congestion and overcrowding in pedestrian traffic may lead to significant inefficiency and safety hazards. Thus, the design of guideway networks that provide a fine balance between traffic congestion and infrastructure construction investment is vital. This paper presents a mathematical formulation and topology optimization framework for paved pedestrian guideway design under physics-based traffic equilibrium in a continuous space. Pedestrians are homogeneous, and their destination and path choices under the Nash equilibrium condition are described by a set of nonlinear partial differential equations. The design framework optimizes the deployment of pavement, which alters the road capacity and directly affects pedestrians' free flow travel speed. A maximum crowd density constraint is included in the design model to address public safety concerns (e.g., over stampede risks). A series of numerical experiments are conducted to illustrate the effectiveness of the proposed model as well as solution techniques. The proposed framework, which builds on the traffic equilibrium theory, produces optimized guideway designs with controllable maximum pedestrian density, accounts for budget constraints (through an adjustable multiplier that balances pavement construction and travel costs), and allows for control of the spatial configuration of road branches. Comparison with lamellar structures and more conventional guideway designs demonstrates better performance of the outcomes from the proposed modeling and optimization framework.

 $\textbf{Keywords} \ \ \text{Topology optimization} \cdot \text{Guideway network design} \cdot \text{Continuous traffic equilibrium} \cdot \text{Transportation engineering} \cdot \text{Nash equilibrium}$

1 Introduction

Topology optimization is a powerful computational design method for finding optimized shapes and placement of material within a prescribed design domain to obtain improved performance (Sigmund and Maute 2013; Deaton and Grandhi 2014). This method has been used in a wide rangeof disciplines with various physical laws, including structural engineering (see, e.g., Sigmund and Maute 2013; Bendsøe and Kikuchi 1988; Beghini et al. 2014; Zhang

Responsible Editor: Mehmet Polat Saka

- Department of Civil and Environmental Engineering, University of Illinois at Urbana Champaign, 205 North Mathews Ave, Urbana, IL 61801, USA
- Department of Mechanical Science and Engineering, University of Illinois at Urbana Champaign, 1206 W. Green St, Urbana, IL 61801, USA

et al. 2017, 2018), aerospace engineering (e.g., Maute and Allen 2004; Zhu et al. 2016; Aage et al. 2017), fluid mechanics (e.g., Borrvall and Petersson 2003; Alexandersen and Andreasen 2020; Alexandersen et al. 2016), material design (e.g., Sigmund 1994, 1995; Xia and Breitkopf 2015; Wang et al. 2014; Clausen et al. 2015), photonic design (e.g., Wang et al. 2018; Christiansen et al. 2019), and fracture resistance design (e.g., Da et al. 2018; Russ and Waisman 2020). Depending on the type of elements used, topology optimization can be classified into discrete and continuum types. The density-based approach (Bendsøe and Sigmund 2003), one of the commonly used methods of the continuum type, optimizes material by redistributing the density of each continuum element.

In this study, we propose a continuum topology optimization framework to design pavement guideway networks to serve pedestrian traffic. When pedestrian traffic goes to a set of service facilities (i.e., the actual points of interest), presence of *guideways* could collectively form a structure of channels along which travel speed and/or direction can be altered. The design of pedestrian guideways is of great



importance. Without proper flow channelization, pedestrian traffic may experience overcrowding that imposes both inefficiency and safety hazards. Examples include the devastating stampede incidents in recent years, Shanghai's New Year Eve crash in 2014 that killed 36 people and severely injured 47 others (BBC News 2015), and the 2015 Hajj pilgrimage incident in Mina, Saudi Arabia, that killed at least 2411 pilgrims (Gladstone 2015).

Design of transportation networks under congestion has received a lot of attention, but mostly in the discrete setting, e.g., shipment routing problems under congestion (Bai et al. 2011, 2016; Hajibabai and Ouyang 2013; Hajibabai et al. 2014), shelter network design problems (Sherali et al. 1991; Li et al. 2012; An et al. 2015), and competitive supply chains (Konur and Geunes 2011, 2012). We normally assume that the routing decisions of individuals reach a Nash equilibrium in the steady-state. Meanwhile, the designer considers altering the topology of the guideway network (e.g., by addition, expansion, reduction, or removal of capacity), knowing that the travelers will react to the network alternation. The design problem, often involving a bi-level leader-follower decision structure, aims at minimizing certain system-wide cost at the upper level, while satisfying traffic equilibrium at the lower level. Such bilevel design problems are among the most difficult to solve due to their nonlinear, nonconvex, and mixed-integer forms.

Unlike vehicles, moving pedestrians do not always follow predetermined lanes. Hence, using a discrete network (even a very dense one) to approximate pedestrian crowd concentration and congestion may not always be satisfactory. Difficulties are often associated with handling (i) the coupling of congestion experienced by neighboring travelers in different travel directions, and (ii) clustering of twodimensional fluxes into one-dimensional link flows and the characterization of link properties. These challenges motivate researchers to develop alternative modeling approaches such as those that can directly describe traffic in a twodimensional continuous space. Yang et al. (1994), Yang (1996), and Yang and Wong (2000) first formulate a user equilibrium model to describe congested traffic in a continuous space via a set of nonlinear partial differential equations. Wang (2017), Wang and Ouyang (2016), and Wang et al. (2019) further show that for bounded and simply connected spatial domains, traffic equilibrium is equivalent to the well-known Neumann problem in the mathematics literature (Guenther and Lee 1996), and solution to equilibrium can be expressed in explicit closed forms for some specific domains. In a continuous space, guideways can also be deployed continuously to influence traffic path choices. The optimal provision of guideways, either through natural evolution or systematic design, has been an intriguing problem (Helbing et al. 2005; Helbing Dirk and Molnar 1997), and some preliminary efforts have been made in this direction.

Most existing work has focused on barrier design. For example, Johansson and Helbing (2007) and Jiang et al. (2014) used a combination of genetic algorithm and agent-based simulations (e.g., social force model, Helbing 1991; Helbing and Molnar 1995 to optimize the architectural features that can improve pedestrian flow under evacuation.

There is a lack of effective modeling and solution methodologies for pavement guideway design under induced traffic congestion at equilibrium. On the modeling side, the majority of work conducted so far has either focused on systems with an underlying discrete network topology that are inadequate for pedestrian traffic, or used simplified PDEs that may not accurately describe continuous traffic equilibrium. In addition, the maximum crowd density constraint, which is vital for safety control, has not been incorporated into existing continuous guideway optimization models. On the solution side, continuum topology optimization techniques have rarely been applied to transportation problems. Gersborg-Hansen et al. (2006) indicated the potential application of topology optimization to transportation problems. Wadbro and Noreland (2019) recently propose the problem of designing both the guideway capacity and conductivity to facilitate the movement of goods governed by a linear steady-state diffusion-type model (based on an electromagnetic field analogy). Their objective is a weighted sum of the construction and transportation costs. In another transportation-related field, robot path planning, topology optimization has been used to find optimized paths from the starting point to destination in an environment with many obstacles (Ryu et al. 2012). The state equation therein mimics the steady-state heat conduction equation.

Taking into account the aforementioned aspects, this paper establishes holistic traffic modeling and topology optimization frameworks for the design of complex guideway networks that serve congested traffic in a continuous space. The innovation of this study lies in four major aspects.

- First, we propose a general topology optimization framework that allows the design of pavement infrastructure layout, which alters the guideway capacity and the free flow travel speed of the pedestrians. The objective function minimizes the transportation cost with a balance of construction budget (through a shadow price, or a multiplier), which is conceptually similar to augmenting a construction cost penalty to the objective function.
- Second, the formulation is built on a physics-based traffic equilibrium model, i.e., the pedestrians' best destination and path choices in a continuous space are precisely described by a set of nonlinear PDEs based on Nash equilibrium. The resulting optimization problem is nonconvex and its state equations are highly nonlinear. In order to tackle such problems, we present a novel solution strategy that integrates a recently developed fixed-point iteration method and Newton's



method to achieve stable convergence with a relatively low computation cost.

- Third, in order to ensure public safety, we introduce a maximum pedestrian density constraint to the optimization framework.
- Last but not the least, we investigate two types of boundary conditions of the traffic flow problem for different real-life scenarios, with or without explicit control of the exit flow across multiple service facilities.

The proposed framework leads to results that have many applications such as paving trails in grassland and cleaning snow in open grounds.

The remainder of the paper is organized as follows. Section 2 introduces the nonlinear transportation model, based on the Nash equilibrium of travelers, and the general optimization formulation of the pavement layout design problem. Section 3 presents finite element discretization of the transportation model and proposes a topology optimization framework for pedestrian pavement design, including a maximum density constraint. Section 4 presents four numerical examples that discuss various aspects of the proposed framework and solution scheme. Section 5 provides concluding remarks. The paper is complemented by two appendices. Appendix A thoroughly describes the hybrid solution scheme of the nonlinear state equations and Appendix B derives the sensitivity.

2 Transportation model and optimization formulation

This section introduces the continuous model for congested pedestrian traffic based on the Nash equilibrium of travelers, and proposes the general optimization problem. In a compact two-dimensional space $\Omega \subseteq \mathbb{R}^2$, a set of service facilities are located at $\mathbf{x} := \{x_1, x_2, ...\} \subseteq \Omega$. Continuously distributed pedestrian travelers are generated near location \mathbf{x} according to a density function $q(\mathbf{x}), \forall \mathbf{x} \in \Omega$ (per unit time per unit area), and they must visit any one of these facilities to receive service. For facility i, we define $\mathcal{A}_i \subseteq \Omega$ as the subarea from where pedestrians travel to facility i for service.

The transportation cost per unit distance per pedestrian near location $x \in \Omega$ is isotropic but dependent on the local traffic intensity. By properly defining the spatiotemporal units, we assume the free flow travel time per unit distance (i.e., free flow pace, the inverse of free flow speed) is $\eta(x)$, and the extra delay time due to congestion near location x is a polynomial function of the local flux $\mathbf{f}(x)$, i.e., $\left(\frac{|\mathbf{f}(x)|}{\alpha(x)}\right)^{g(x)}$, where $|\cdot|$ is the Euclidean norm, $\alpha(x)$ is

a measure of the local roadway "capacity" near x, and g(x) is a non-negative scalar function that captures the local "sensitivity" to congestion. Following the convention, we assume that positive flux leaves a closed surface, and negative flux enters a closed surface. In addition, traveling a unit distance near location x could incur a monetary cost $b_1(x)$, which is also normalized to have the unit of time. As such, the generalized cost (monetary and time) for a traveler to cover one unit of distance near x is

$$c(\mathbf{x}) = b_1(\mathbf{x}) + \eta(\mathbf{x}) + \left(\frac{|\mathbf{f}(\mathbf{x})|}{\alpha(\mathbf{x})}\right)^{g(\mathbf{x})}$$
(1)

A pedestrian from x chooses to patronize one of the facilities, say facility i, along the best travel path $p(x) \subseteq \Omega$ such that the pedestrian's generalized cost is minimized.² Hence, $x \in \mathcal{A}_i$ if $x_i \in p(x)$ and

$$[i, p(\mathbf{x})] = \arg\min_{i', p'} \int_{p'} c(\mathbf{x}) d\mathbf{x}$$

Clearly, the pedestrian's destination and path choices are coupled through the dependence of c(x) on local flux intensity, which is the outcome of all other pedestrians' collective decisions. Assuming that each pedestrian unilaterally chooses the best option conditional on c(x)—these pedestrians will collectively form a Nash equilibrium³ in the continuous space, such that all pedestrians from location x for obtaining service will experience an equal total generalized cost, which we denote by a scalar function $\phi(x)$ with the unit of time, i.e.,

$$\phi(\mathbf{x}) = \int_{p(\mathbf{x})} c(\mathbf{x}) d\mathbf{x}, \forall \mathbf{x} \in \mathcal{A}_i$$

Yang and Wong (2000) showed that the KKT conditions for the pedestrians' Nash equilibrium can be described as follows:

$$c(x)\frac{\mathbf{f}(x)}{|\mathbf{f}(x)|} = -\nabla\phi(x), \forall x \in \Omega,$$
(2)

$$\nabla \cdot \mathbf{f}(\mathbf{x}) + q(\mathbf{x}) = 0, \forall \mathbf{x} \in \Omega, \tag{3}$$

$$\mathbf{f}(\mathbf{x}) \cdot \mathbf{n}(\mathbf{x}) = \bar{q}(\mathbf{x}), \forall \mathbf{x} \in \partial \Omega, \tag{4}$$

$$\phi(\mathbf{x}) = 0, \forall |\mathbf{x} - \mathbf{x}_i| \le r_0, \forall i \tag{5}$$

where ∇ is the gradient operator, \cdot is the inner product operator, n(x) is the unit normal vector of $\partial \Omega$, and $\bar{q}(x)$

³Also called user equilibrium (UE) in the transportation literature, as originally described in Wardrop (1952).



¹This function form is analogous to the well-known BPR function (U.S. Bureau of Public Roads), but other non-decreasing functions are also acceptable.

²The choice of facility i depends on the pedestrian's location x, i.e., i(x). However, we note that $x \in \mathcal{A}_i$ equivalently indicates the facility choice of the pedestrians at x. Hence, we simply use facility index i without the argument, for notation convenience.

denotes the traffic inflow or outflow at the boundary of the domain. It shall be noted that, due to singularity of flowintensity at x_i , conditions (5) are slightly different from that in Yang and Wong (2000) such that each facility has a non-zero radius of $r_0 \to 0^+$. Ouyang et al. (2015) have also shown that each pedestrian's equilibrium travel path shall strictly remain within the service region of its chosen facility, i.e., $p(x) \subseteq \mathcal{A}_i$ for all $x \in \mathcal{A}_i$, and the set $\{\mathcal{A}_i, \forall i\}$ forms a compact and disjoint service region (except for overlapping boundaries), i.e.,

$$\bigcup_{i=0}^{N} \mathcal{A}_{i} = \Omega \text{ and } \mathcal{A}_{i} \bigcap \mathcal{A}_{j} = \emptyset, \forall i \neq j$$
 (6)

Based on the introduced concepts and variables, we propose a continuous network design optimization problem, whose objective is to find $\alpha(x)$ and the associated $\mathbf{f}(x)$ that minimize the total overall cost, while the pedestrians' facility and travel choices are described by (1)–(6). Local capacity $\alpha(x)$ can be altered by changing the ground surface, e.g., from unpaved soil or lawn to gravel or asphalt/ concrete pavements, or sweeping snow to form clean trails, such that the increased capacity comes through increased free flow travel speed (or decreased free flow pace $\eta(x)$). Physically, the presence of the pavement construction at location x increases the road capacity at x from α_0 to α , where α_0 is the initial condition before any construction. In such a case the local free flow speed shall be proportional to the value of $\alpha(x)$; e.g., the formula for c(x) becomes

$$c(\mathbf{x}) = b_1(\mathbf{x}) + \frac{b_2}{\alpha(\mathbf{x})} + \left(\frac{|\mathbf{f}(\mathbf{x})|}{\alpha(\mathbf{x})}\right)^{g(\mathbf{x})},\tag{7}$$

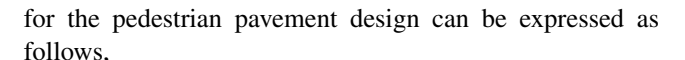
for some constant b_2 . The local pedestrian density near x, denoted $\rho(x)$, is given by the product of flux intensity and the pace; i.e.,

$$\rho(\mathbf{x}) = |\mathbf{f}(\mathbf{x})| \cdot \left[\frac{b_2}{\alpha(\mathbf{x})} + \left(\frac{|\mathbf{f}(\mathbf{x})|}{\alpha(\mathbf{x})} \right)^{g(\mathbf{x})} \right]$$
(8)

In light of safety concerns associated with overcrowding, we impose that the density of pedestrians in all neighborhoods be bounded by an upper bound ρ_{max} ; i.e.,

$$\rho(\mathbf{x}) \le \rho_{\text{max}} \tag{9}$$

We assume that the prorated cost per unit time for setting a capacity of $\alpha(x)$ for a unit area near x is given by a function $f(\alpha(x))$. For notation convenience, we further define $\alpha = \{\alpha(x), \forall x\}, \ \mathbf{f} = \{\mathbf{f}(x), \forall x\}, \ \phi = \{\phi(x), \forall x\}, \ \rho = \{\rho(x), \forall x\}, \ \mathcal{A} = \{\mathcal{A}_i, \forall i\}.$ The optimization formulation



$$\min_{\alpha, \mathbf{f}, \rho, \mathcal{A}} \sum_{i=1}^{N} \int_{\mathbf{x} \in \mathcal{A}_{i}} [f(\alpha(\mathbf{x})) + C_{T}\phi(\mathbf{x})q(\mathbf{x})]d\mathbf{x}$$
 (10)

s.t.
$$\sum_{i=1}^{N} f(x_i) \le B|\Omega|$$
 (11)
$$\alpha, \mathbf{f}, \phi, \rho, \mathcal{A} \text{ satisfy } (2) - (9), \forall \mathbf{x} \in \Omega, \forall i$$

The integrand in the objective function captures the "net" costs of constructing pavements in the area so as to have capacity $\alpha(x)$, and those of travel cost experienced by all pedestrians who start their trip in a unit time, $\int_{\Omega} [\phi(x)q(x)]dx$. Coefficient C_T is the monetary value of one unit pedestrian time. When $b_1(x) = 0$, $\forall x$, per Little's (1961) Law, the latter term in the integrand can be equivalently expressed as $C_T \int_{\Omega} \rho(x) dx$. This substitution will be used in the next section to develop density-based topology optimization reformulation. Constraint (11) enforces a budget constraint for pavement construction.

3 Finite element approximation and topology optimization formulation

In this section, we introduce the finite element (FE) discretization of the nonlinear state equations that describe the countinuous transportation model in Section 2. Using the density-based approach, we then derive the corresponding continuous and discretized topology optimization formulations. For conciseness, we drop the location argument \boldsymbol{x} in all expressions from here forward.

3.1 Finite element discretization of the transportation model

We introduce a new variable κ to rewrite the original PDEs to simplify the notation,⁴ such that

$$\kappa := \frac{|\mathbf{f}|}{c} \tag{12}$$

By plugging the expression of the local generalized cost c from (7) into (12), we obtain

$$\kappa = \kappa_{\min} + \frac{|\mathbf{f}|}{b_1 + \frac{b_2}{\alpha} + \left(\frac{|\mathbf{f}|}{\alpha}\right)^g},\tag{13}$$

⁴Wadbro and Noreland (2019) used an interesting linear heat conduction model analogy to approach a similar problem; i.e. it assumes a linear relation between the local flux $\mathbf{f}(x)$ and the potential gradient $\nabla \phi(x)$ with a constant conductivity factor κ . The model we introduced in (16)–(19), based on the Nash equilibrium condition of travelers in the continuous domain, shows that the κ in (17) should be a nonlinear function of $|\nabla \phi|$, see (15).



where κ_{min} is a small positive number added to (13) to ensure the resulting model is well-posed so that the solution procedure of the nonlinear state equation can be facilitated. With the introduction of κ , we rewrite (2) as

$$\mathbf{f} = -\kappa \nabla \phi \tag{14}$$

The relations (12) and (13) implicitly define κ as a nonlinear function of α and $|\nabla \phi|$. To this end, we plug (14) into (13) to obtain

$$\left[\left(1 - \frac{\kappa_{\min}}{\kappa} \right) b_1 - |\nabla \phi| \right] \alpha^g + \left(1 - \frac{\kappa_{\min}}{\kappa} \right) b_2 \alpha^{(g-1)} + \left(1 - \frac{\kappa_{\min}}{\kappa} \right) (\kappa |\nabla \phi|)^g = 0 \quad (15)$$

For given b_1 , b_2 , and g, (15) defines an implicit nonlinear mapping from α and $|\nabla \phi|$ to κ . The state equations (2)–(5) can then be expressed equivalently as follows:

$$\nabla \cdot \mathbf{f} + q = 0 \quad \text{in } \Omega, \tag{16}$$

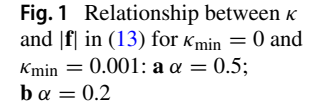
$$\mathbf{f} = -\kappa \nabla \phi \quad \text{in } \Omega, \tag{17}$$

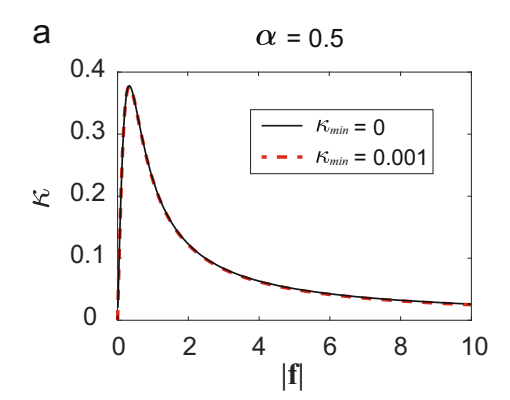
$$\phi = 0 \quad \forall |\mathbf{x} - \mathbf{x}_i| \le r_0, \forall i, \tag{18}$$

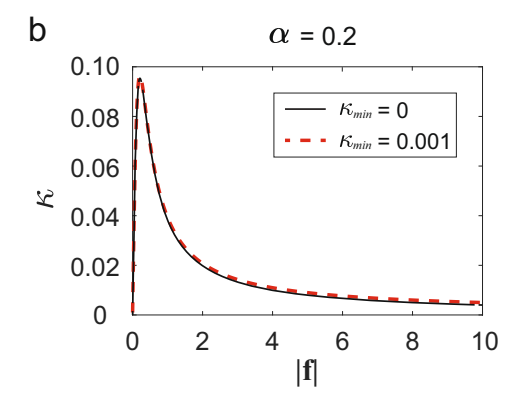
$$\mathbf{f} \cdot \mathbf{n} = \bar{q} \quad \text{on } \partial \Omega \tag{19}$$

where n is the unit normal vector of $\partial \Omega$, and \bar{q} denotes the traffic inflow or outflow at the boundary of the domain.

To comprehend the nonlinear dependence of κ on $|\mathbf{f}|$ and $\nabla \phi$ defined by (13)–(15), as well as evaluating the influence of κ_{\min} , we plot κ versus $|\mathbf{f}|$ in Fig. 1, and κ versus $\nabla \phi$ in Fig. 2. We first observe that both figures demonstrate nonlinear relationships among the variables in (17). Figure 1 shows that, for both $\alpha=0.5$ and $\alpha=0.2$, no obvious difference is observed between the curves with and without κ_{\min} , indicating κ_{\min} has a negligible influence on the κ vs. $|\mathbf{f}|$ curve. From Fig. 2a, we observe that, without κ_{\min} , a discontinuity exists near $\nabla \phi=0$. This discontinuity can be problematic for nonlinear FE methods (e.g., using Newton's method (Zhang et al. 2017)) because the initial guess is typically $\phi=0$ and $\nabla \phi=0$. However, by adding κ_{\min} (both $\kappa_{\min}=0.001$ and $\kappa_{\min}=0.01$ in Fig. 2b and c, respectively), the initial discontinuity in the $\kappa_{\min}=0$ case









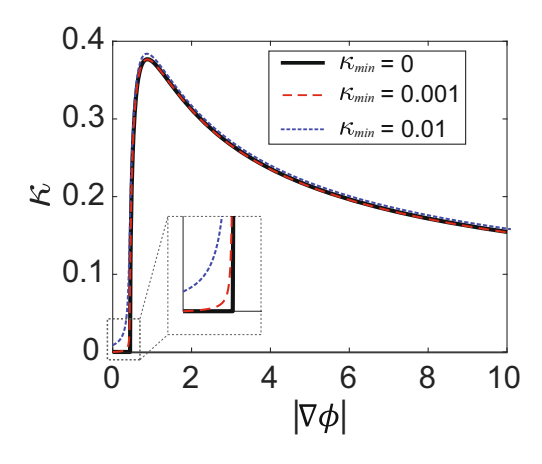


Fig. 2 Relationship between κ and $\nabla \phi$ defined by (15) for $\kappa_{\rm min}=0$, $\kappa_{\rm min}=0.001$, and $\kappa_{\rm min}=0.01$

is smoothened away while the overall shape of the curve stays unchanged. Thus, based on Figs. 1 and 2, we remark that adding a small κ_{min} value prevents numerical issues while having little influence to the behavior of the model. For numerical examples in Section 4, we gradually reduce the value of κ_{min} to further reduce of its influence.

For the set of PDEs given in (16)–(19), the corresponding weak form consists of finding $\phi \in \mathcal{H}_1(\Omega)$ such that

$$\int_{\Omega} \nabla \psi \cdot (\kappa(\alpha, |\nabla \phi|) \nabla \phi) d\mathbf{x} = \int_{\partial \Omega} \psi \bar{q} ds + \int_{\Omega} \psi q d\mathbf{x}, \quad \forall \psi \in \mathcal{U}^{0},$$
(20)

where $\mathscr{H}_1(\Omega)$ is the standard Sobolev space consisting of functions whose weak derivatives up to the 1st order are square-integrable on Ω ; ψ is the test function; and \mathscr{U}^0 stands for the space of the test function as follows,

$$\mathcal{U}^0 = \{ \phi \in \mathcal{H}_1(\Omega) : \phi = 0 \ \forall |x - x_i| \le r_0, \forall i \}$$
 (21)

Then, we introduce a partition of the domain Ω into a total of n non-overlapping elements with M nodes, namely, $T_h = \{E_\ell\}_{\ell=1}^n$, where T_h is a partition and E_ℓ is the area

of element ℓ . On T_h , we introduce a finite-dimensional subspace \mathcal{U}_h of \mathcal{U} , and approximate ϕ and ψ as

$$\phi_h = \sum_{i=1}^{M} \Phi_i N_i \text{ and } \psi_h = \sum_{i=1}^{M} \Psi_i N_i,$$
 (22)

respectively. Here N_i is the global Lagrange basis function of \mathscr{U}_h associated with the ith node, and Φ_i and Ψ_i are degrees of freedom (DOFs) of ϕ_h and ψ_h on that node, respectively. Next, we adopt piecewise constant approximations of the road capacity α and the nonlinear variable κ . More specifically, the road capacity α_ℓ is a constant for element ℓ , which is discussed in detail later; and κ_ℓ is computed via $\kappa_\ell(\alpha_\ell, |\nabla_{E_\ell}\phi_h|)$ and is also a constant for element ℓ , where $\nabla_{E_\ell}\phi_h$ is the area average of $\nabla\phi_h$ over E_ℓ , namely, $\nabla_{E_\ell}\phi_h \doteq 1/|E_\ell|\int_{E_\ell}\nabla\phi_h d\mathbf{x}$, and $\kappa_\ell(\alpha_\ell, |\nabla_{E_\ell}\phi_h|)$ is the implicit mapping defined by the nonlinear function (13). In a vector representation, $\nabla_{E_\ell}\phi_h$ can be written as

$$\nabla_{E_{\ell}}\phi_{h} = \mathbf{G}_{\ell}\boldsymbol{\Phi},\tag{23}$$

where G_{ℓ} is a matrix whose *i*th column is given by

$$[\mathbf{G}_{\ell}]_{:,i} = \int_{E_{\ell}} \nabla N_i \, d\mathbf{x}, \tag{24}$$

and $\Phi = (\Phi_i)_{i=1}^M$ is the vector of nodal potentials. Accordingly, $|\nabla_{E_i} \phi_h|$ is given by

$$|\nabla_{E_{\ell}}\phi_{h}| = \sqrt{\boldsymbol{\Phi}^{T}\mathbf{G}_{\ell}^{T}\mathbf{G}_{\ell}\boldsymbol{\Phi}} = \sqrt{\boldsymbol{\Phi}^{T}\mathbf{M}_{\ell}\boldsymbol{\Phi}}, \text{ with } \mathbf{M}_{\ell} = \mathbf{G}_{\ell}^{T}\mathbf{G}_{\ell}$$
(25)

We note that, in practice, both matrices G_{ℓ} and M_{ℓ} need to be computed only once throughout the optimization for each element in the mesh. Having introduced the discretization T_h , the Galerkin approximation of the continuous weak form (20) becomes seeking $\phi_h \in \mathcal{U}_h$ such that

$$\sum_{i=1}^{n} \int_{E_{i}} \nabla \psi_{h} \cdot \left(\kappa_{\ell}(\alpha_{\ell}, |\nabla_{E_{\ell}} \phi_{h}|) \nabla \phi_{h} \right) d\mathbf{x}$$

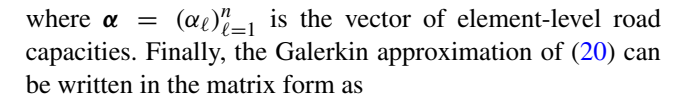
$$= \langle \bar{q}, \psi_{h} \rangle_{h} + \langle q, \psi_{h} \rangle_{h}, \quad \forall \psi_{h} \in \mathcal{U}_{h}, \tag{26}$$

where the first and the second terms on the right-hand side stand for standard FE approximations of the terms related to the boundary inflow/outflow \bar{q} and q, respectively. To obtain a matrix representation, we first define a local matrix

$$[\mathbf{k}_{\ell}^{0}]_{ij} = \int_{E_{\ell}} \nabla N_{i} \cdot \nabla N_{j} d\mathbf{x}$$
 (27)

Since κ is assumed to be constant within each element, we can compute the global matrix corresponding to the left-hand side of (26) as

$$\mathbf{K}^{\alpha} \Big(\kappa(\boldsymbol{\alpha}, \boldsymbol{\Phi}) \Big) = \sum_{\ell=1}^{n} \kappa_{\ell}(\alpha_{\ell}, |\nabla_{E_{\ell}} \phi_{h}|) \mathbf{k}_{\ell}^{0}, \tag{28}$$



$$\mathbf{K}^{\alpha} \Big(\kappa(\boldsymbol{\alpha}, \boldsymbol{\Phi}) \Big) \boldsymbol{\Phi} = \boldsymbol{Q}, \tag{29}$$

where Q stands for the vector representation of terms on the right-hand side of (26). We define a global residual vector R as:

$$R(\alpha, \Phi) = \mathbf{K}^{\alpha} \Big(\kappa(\alpha, \Phi) \Big) \Phi - Q = \mathbf{0}$$
 (30)

The above system of equations (29) is highly nonlinear and challenging to solve using the standard Newton's method for two main reasons. First, in the Newton's method, an initial guess of $\Phi = 0$ is typically used, which corresponds to $|\nabla_{E_{\ell}}\phi_h|=0$ for all the elements in the mesh. In such cases, according to Fig. 2, the corresponding κ for each element will be close to zero, leading to an ill-conditioned matrix $\mathbf{K}^{\alpha}(\kappa)$. This ill-conditioning will not be resolved even if a non-zero uniform initial guess for Φ is used, because $|\nabla_{E_{\ell}}\phi_h|$ for all the elements will still be zero. Second, because of the high nonlinearity of the state equation, the standard Newton's method may fail to converge even when the initial guess of the current design step takes the solution from the previous step. To address the above challenges and achieve stable convergence, we propose a hybrid strategy that combines a recently developed fixedpoint iteration method, Alternating Anderson Richardson (AAR) (Survanarayana et al. 2019; Banerjee et al. 2016), and Newton's method. The idea is to first use the AAR method to bring the iterate close to the solution and then employ the Newton's method to achieve fast convergence. The proposed hybrid strategy is shown to be robust and efficient, because it combines advantages of both the AAR and the Newton's methods: the AAR method is stable and can effectively reduce the residual even when the search point is far away from the solution; however, it does not have second-order convergence, whereas the Newton's method converges at the second-order but only when the current iterate is close enough to the solution. The description of this hybrid nonlinear solution strategy is provided in Appendix A.

3.2 Topology optimization formulations

Here, we propose a continuous topology optimization formulation of the guideway design problem (10). The goal is to find the optimized distribution of pavement construction in order to improve local traffic capacity (through the increase of free flow travel speed), so that the overall construction and travel cost is minimized subject to density upper bound ρ_{max} . The design field is the road capacity α . We denote parameters α_0 and α_{max} as the initial pavement capacity (before construction) and the maximum



possible capacity, respectively. Variable $\alpha(x) \in [\alpha_0, \alpha_{\max}]$ is the road capacity after pavement construction at location x. Moreover, we define the pavement construction cost per unit time of its life cycle and total travel cost (assuming $b_1(x) = 0, \forall x$) as

$$J_R(\alpha) = \int_{\Omega} f(\alpha(\mathbf{x})) d\mathbf{x} = C_R \int_{\Omega} (\alpha - \alpha_0) d\mathbf{x}, \tag{31}$$

and

$$J_T(\rho(\alpha,\phi_\alpha)) = C_T \int_{\Omega} \rho(\alpha,\phi_\alpha) dx, \tag{32}$$

where C_R is a parameter capturing the prorated unit cost for road construction. We propose the following continuous topology optimization formulation to capture the pavement design problem:

$$\min_{\alpha \in \mathcal{L}_{\infty}(\Omega; [\alpha_{0}, \alpha_{\max}])} \left\{ J(\alpha) = \beta J_{R}(\alpha) + J_{T}(\rho(\alpha, \phi_{\alpha})) \right\}
\text{s.t.} \quad \rho(\alpha, \phi_{\alpha}) - \rho_{\max} \leq 0, \quad \forall \mathbf{x} \in \Omega,
\text{with} \quad \phi_{\alpha} \text{ being the solution to } (2) - (5), (7),$$
(33)

with the expression of $\rho(\alpha, \phi)$ given by

$$\rho(\alpha, \phi) = |\nabla \phi| \kappa(\alpha, |\nabla \phi|) \left[\frac{b_2}{\alpha} + \left(\frac{|\nabla \phi| \kappa(\alpha, |\nabla \phi|)}{\alpha} \right)^g \right], \tag{34}$$

where we recall that $\kappa(\alpha, |\nabla \phi|)$ is defined implicitly through (15). In the above optimization formulation, instead of minimizing the direct weighted summation of pavement construction cost and the pedestrian transportation cost subject to a construction budget constraint, we introduce a non-negative multiplier $\beta \geq 0$ to the first term. It captures the fact that most real-world infrastructure investment decisions are subject to binding budget constraints. Hence, β can be interpreted as the shadow price of such a budget constraint, which turns out to be unitless, with a larger value indicating a tighter budget.

Using the FE discretization introduced in Section 3.1, the discretized topology optimization formulation has the following form:

$$\min_{z \in [z_0, z_{\text{max}}]^n} \left\{ J(\boldsymbol{\alpha}, \boldsymbol{\rho}(\boldsymbol{\alpha}, \boldsymbol{\Phi})) = \beta C_R \mathbf{v}^T \boldsymbol{\alpha} + C_T [\mathbf{v}^T \boldsymbol{\rho}(\boldsymbol{\alpha}, \boldsymbol{\Phi})] \right\}$$
(35)

s.t.
$$\left(\sum_{\ell=1}^{n} \left(\rho_{\ell}(\alpha_{\ell}, \boldsymbol{\Phi})\right)^{p_{n}}\right)^{1/p_{n}} - \rho_{\max} \leq 0$$
 (36)

with
$$\mathbf{R}(\boldsymbol{\alpha}, \boldsymbol{\Phi}) = \mathbf{0}$$
 and $\boldsymbol{\alpha} = \mathbf{P}z$ (37)

In the above formulation, $z = (z_\ell)_{\ell=1}^n$, $\alpha = (\alpha_\ell)_{\ell=1}^n$, $\rho = (\rho_\ell)_{\ell=1}^n$, $\kappa = (\kappa_\ell)_{\ell=1}^n$ and $\mathbf{v} = (|E_\ell|)_{\ell=1}^n$ are vectors of design variable, road capacity, pedestrian density, conductivity, and element areas, respectively. Parameters z_0

and z_{max} are the lower and upper bounds of the design variable, which are set to α_0 and α_{max} respectively. A density filter (Bourdin 2001), which is represented by matrix **P**, is applied to regularize the optimization problem and provide a control on the length scale of the load capacity field α . To circumvent the large number of local, elementwise constraints, we adopt the p-norm approach (Duysinx and Sigmund 1998) with p_n denoting the chosen norm. The derivation of the sensitivity information of both the objective and constraint is given in Appendix **B**.

4 Numerical examples

In this section, we present four numerical examples to demonstrate the proposed topology optimization framework for continuous pavement layout design. The first example studies the influence of the total pedestrian flow throughput and the multiplier (β) of the budget constraint on the optimized pavement designs. The second example explores the interplay and interaction between the total pedestrian flow throughput and the upper bound of pedestrian density $\rho_{\rm max}$. The third example studies the impacts of the budget constraint multiplier on the optimized results. In the fourth example, we investigate two types of outflux boundary conditions, which reflect two distinct design scenarios, and compare their influence on the optimized pavement designs. The effect of various filter radius sizes is also studied in the last design example.

For all the examples, the nonlinear state equation is solved by the proposed hybrid solution scheme based on the AAR method and Newton's approach (see Appendix A for details). In addition, a continuation of κ_{min} is adopted as follows: κ_{min} is initialized as $\kappa_{min}=0.1$ and is reduced by half in every optimization step until $\kappa_{\min} = 10^{-3}$. The continuation eases the kink of the nonlinear model (see Fig. 2) in the first few optimization steps. We note that although applying the continuation (before κ_{min} reduces to 0.001) changes the optimization problem and alters the search path, the impact is mostly limited within the first seven steps, as κ_{\min} will reach and stay at 0.001 after the 7th step. The design at the 7th step can be viewed as an initial guess for the subsequent steps. Design variable update in all the examples is handled by the Method of Moving Asymptotes (MMA) (Svanberg 1987). The optimization is considered converged at step k if either the change in design variable $||z_k - z_{k-1}||_{\infty} / \max(z_{k-1})$ drops below a prescribed tolerance $\tau_{\text{opt}} = 10^{-2}$, or the maximum optimization iteration number $N_{\text{max}} = 400$ is reached. The upper bound on the design variables (i.e., maximum pedestrian flux on paved concrete), per Hoogendoorn et al. (2011), is $z_{\text{max}} =$ $\alpha_{\text{max}} = 0.5$ (pedestrians/ft-s) for all examples. The initial guess is $z_{\text{ini}}^{(e)} = 0.3$.



4.1 Example 1: Twin path design

The first example intends to show how the optimized pavement design varies with the total demand throughput and the multiplier of the budget constraint. The first example considers a square design domain (150 ft \times 150 ft). The boundary conditions (traffic inflows at sources and outflows at sinks) and FE mesh are shown in Fig. 3. Traffic from the two sources on the bottom moves toward the two sinks on the top. Each source and sink occupies a small circular area with radius 1/64L. The domain is discretized into a 256×256 FE mesh with 65,536 continuum quadrilateral (Q4) elements and 66,049 degrees of freedom (DOFs).

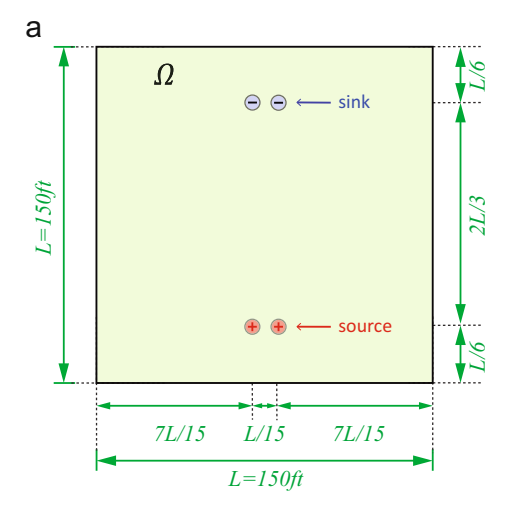
In this example, we investigate the following total demand throughput values that enter from both sources: 1.0, 2.5, and 5.0 (pedestrians per second); and the following values of multiplier/shadow price $\beta = 1000$; 5000; and 10,000. The upper bound of the local pedestrian density ρ_{max} is set as infinity so the density constraint is not active. We use the following model parameters: $C_R = 1$ (\$/ft²year), $C_T = 15,000$ (\$/ft²-year), $b_1 = 0, b_2 = 0.22$, g = 2. All parameters are estimated based on the following information: pavement construction costs about \$7.5 per sqft (https://www.improvenet.com/r/costs-and-prices/ asphalt-paving-cost), for a life cycle of 10 years. Investment are discounted over time at about 5% per year. The guideway systems serve traffic on 250 weekdays per year, with 6 h of peak traffic per day, and the pedestrians value their time at \$10 per hour. The pedestrians can reach a maximum speed of 1.5 (m/s), maximum density of 8 (persons/m²) and a maximum flux of 1.5 (persons/m-s); and when flux reaches 1/3 of capacity, the speed reduces to about 40% of free-flow speed (Hoogendoorn, 2015). The lower bound on the design variables is set as $\alpha_0 = 0.01$, indicating near-zero traffic capacity before pavement construction). In the optimization algorithm, the density filter radius is set to be $R = 1.5h_e = 0.88$, where h_e represents element width.

Figure 4 shows the optimized designs, as well as the corresponding transportation $\cot(J_T)$ and pavement construction $\cot(J_R)$, under the three demand throughputs and three multiplier values. For any given β value, higher demand leads to more pavement construction. This phenomenon is expected because higher transportation costs/congestion naturally require more roadway construction. The increase of J_R is slower than the increase of demand as a balance between J_T and J_R ; e.g., when demand throughput increases by a factor of 5 (i.e., from 1 to 5), J_R only doubles. As a result, J_T also increases by less than a factor of 5.

Under low demand, as β decreases (budget increases), the optimization model tends to increase pavement construction (and as a result, the transportation cost decreases), mainly through thickening of the roads almost monotonically. When β is sufficiently small, the roads start to "merge" into a curvy shape along the direction of expected fluxes that could mitigate congestion. When the demand is relatively high, the roads are thick enough to surround the traffic sources and sinks in all directions. This allows maximum trip dispersion near these concentration points where congestion is most prominent.

Before moving on to additional examples, we perform a parameter cross-check to the designs in Fig. 4 as a final caution. Each of the nine shown designs (optimized with the given set of parameters) is reevaluated under all nine considered parameter sets, and the results are given in Table 1. The italic values along the diagonal are the smallest in each respective column, indicating that, as expected, the design optimized with the same set of parameters has the best performance among all nine designs. This suggests that the proposed optimization model has performed reasonably in terms of yielding optimized designs.

Fig. 3 Example 1. **a** Design domain and boundary conditions; **b** finite element mesh using a 256 × 256 grid



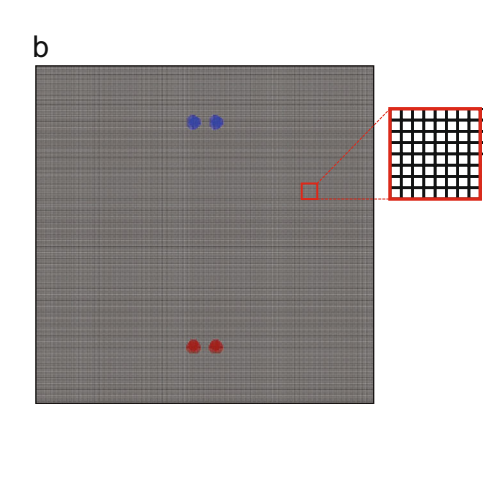
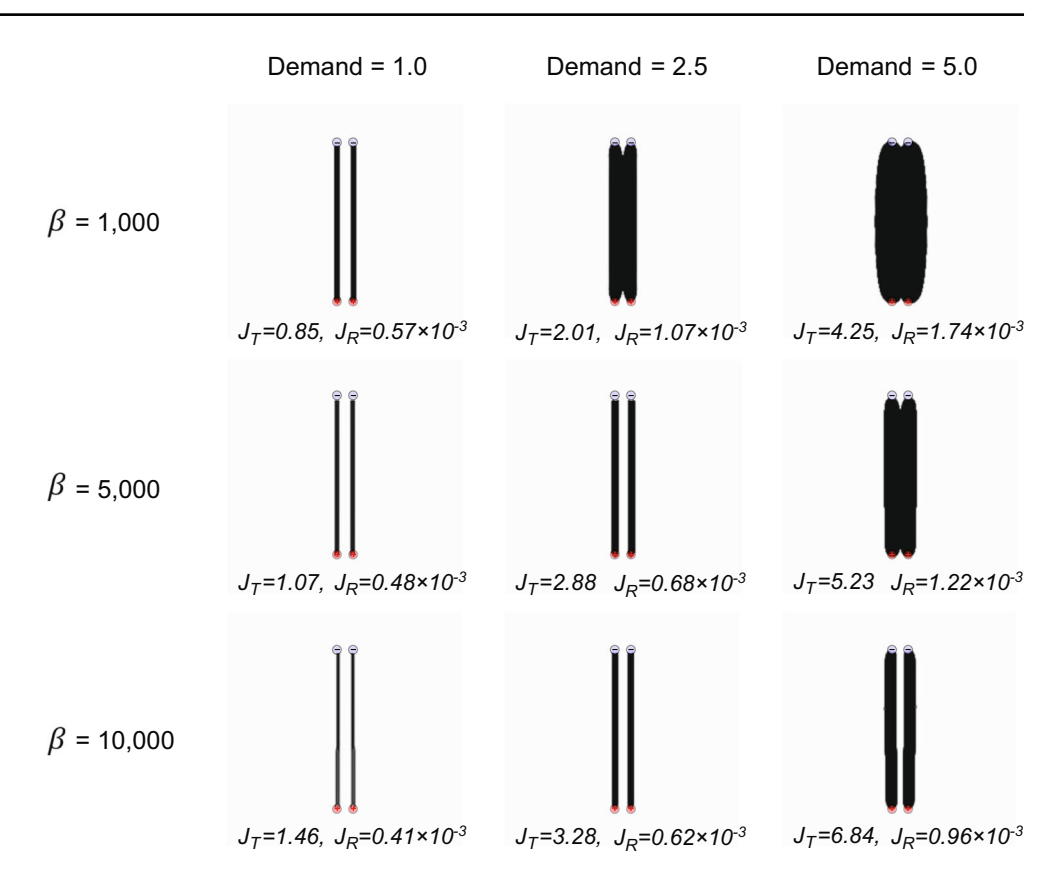




Fig. 4 Example 1: optimized pavement construction designs



4.2 Example 2: Three-lane design

The second example investigates the joint influence of demand throughput and the maximum density ρ_{max} on the topology of the optimized pavement design as well as the overall distribution of traffic flow. The design domain (150 ft \times 150 ft), boundary conditions (sources and sink), and FE mesh are shown in Fig. 5. Traffic from the three sources on the right moves toward the single sink on the left.

The sink and sources each cover a circular area with radius 1/32L. The problem is discretized with the same FE mesh as that for Example 1.

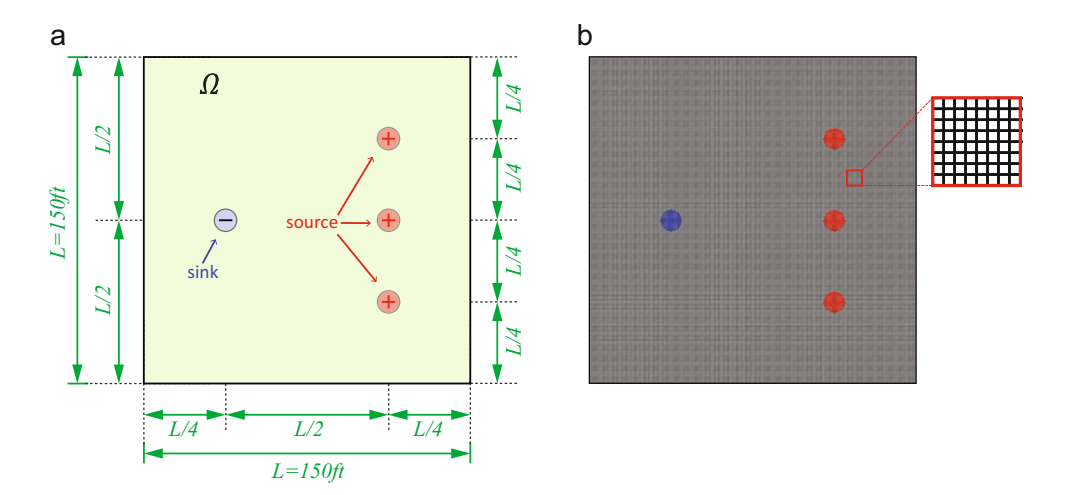
In this example, the total demand throughput varies from 2.5, 5.0, to 7.5 (pedestrians per second), and the maximum density limit ρ_{max} varies from 0.55, 1.0, to ∞ (person/sqft). The shadow price is assumed to be $\beta=4000$. As in Example 1, the unit cost parameters are set to $C_R=1$ (\$/ft²-year) and $C_T=15,000$ (\$/ft²-year); and the model

Table 1 Cross check of optimized designs and parameters in Fig. 4

Design		Tested parameters								
		$\beta = 1000$			$\beta = 5000$			$\beta = 10,000$		
		D=1	D = 2.5	D=5	D=1	D = 2.5	D=5	D=1	D = 2.5	D=5
$\beta = 1000$	D = 1	1.61	4.75	20.68	3.89	7.03	22.96	6.74	9.88	25.81
	D = 2.5	1.91	3.25	7.25	6.21	7.55	11.55	11.58	12.92	16.93
	D = 5	2.55	3.67	6.15	9.52	10.64	13.12	18.23	19.35	21.83
$\beta = 5000$	D = 1	1.78	6.84	33.42	3.69	8.75	35.33	6.08	11.14	37.72
	D = 2.5	1.64	3.81	13.80	4.36	6.54	16.53	7.77	9.94	19.93
	D = 5	2.05	3.30	6.66	6.93	8.17	11.54	13.02	14.27	17.64
$\beta = 10,000$	D = 1	2.19	10.76	57.69	3.82	12.40	59.32	5.86	14.44	61.36
	D = 2.5	1.62	4.19	16.85	4.11	6.67	19.34	7.22	9.78	22.45
	D = 5	1.82	3.29	8.09	5.67	7.15	11.94	10.49	11.97	16.76



Fig. 5 Example 2. a Design domain and boundary conditions; b finite element mesh using a 256×256 grid



parameters are taken as $b_1 = 0$, $b_2 = 0.22$, g = 2. The density filter radius is chosen as $R = 4h_e = 1.17$, and the p-norm of the local traffic density constraint takes a value of $p_n = 12$. The lower bound on the design variables (i.e., capacity before pavement construction) is $\alpha_0 = 0.2$ (e.g., road capacity of grass with snow), indicating relatively small difference before and after construction.

Figure 6 shows the optimized designs and the associated total costs J under the three demand throughputs and three density upper bounds. Comparison across these designs suggests that the proposed topology optimization framework effectively captures the influence of the total demand and maximum pedestrian density constraint on the optimized pavement designs. Increase in demand leads to thicker pavement roads, as expected; yet, notice that pavement layout geometry varies with ρ_{max} values. When $\rho_{\text{max}} = 0.55$, for example, as the demand throughput goes from

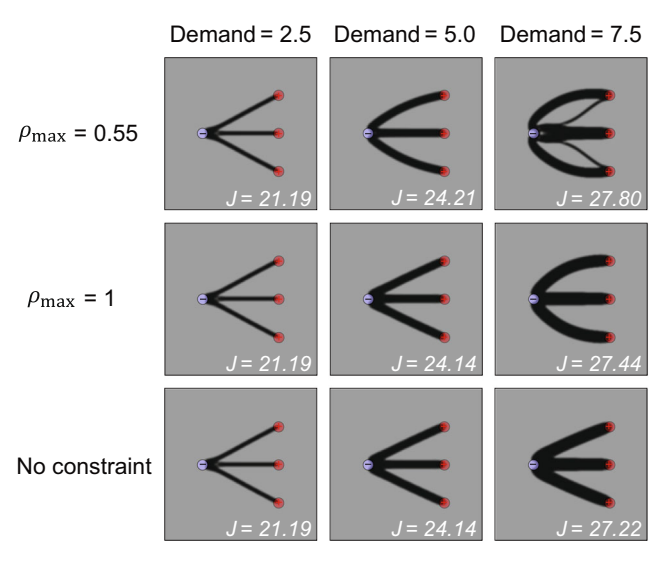
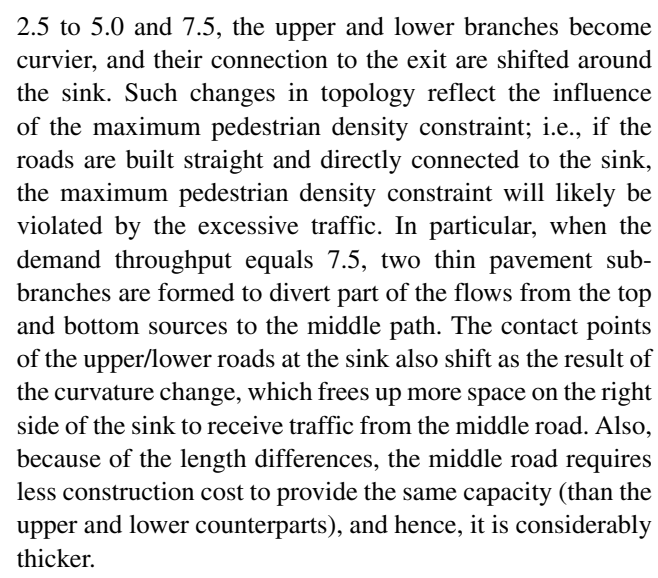


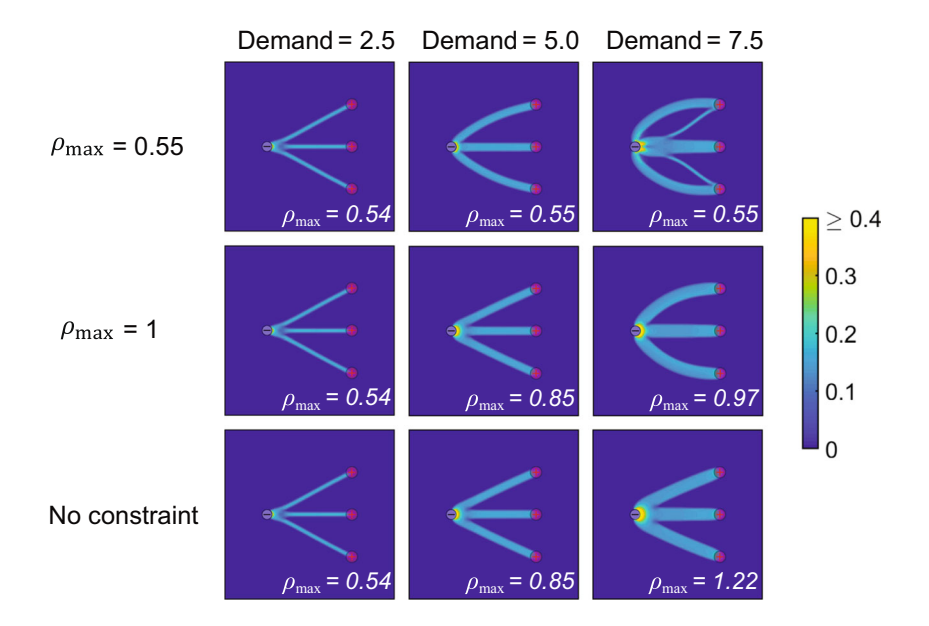
Fig. 6 Example 2: optimized pavement construction design: from left to right varies the total demand throughput, and from top to bottom varies the upper bound of local pedestrian density



When $\rho_{\text{max}} = 1$ and $\rho_{\text{max}} = \infty$, increase of total demand throughput generally results in pavement width changes but no curvature change. This may be because that the maximum density constraint is inactive. When the roads remain straight, the optimizer builds pavements on the shortest paths to save construction cost. When demand = 7.5 and ρ_{max} = 1, however, the maximum density constraint is activated, and both the width and geometry of the paved roads start to change. We emphasize that, with the proposed framework, a maximum density constraint can be satisfied at the expense of a small increase in the total cost. For example, when the demand throughput is 7.5, the total cost of the $\rho_{\text{max}} = 0.55$ case is 2% higher than that of the $\rho_{\text{max}} = \infty$ case. Figure 7 shows the distribution of pedestrian density ρ . In all cases, the highest density is reached at the right side of the sink. This explains why the paved roads from the optimizer tend to curve around the sink under tight density constraints. It is also interesting to observe that the optimized design appears to have more or less constant density ρ in most of the paved



Fig. 7 Example 2: distribution of final pedestrian densities corresponding to the optimized designs



areas. This is reasonable because in congested traffic, the monotonicity of pace function $c(\mathbf{f}(x))$ dictates that density strictly increases with flux intensity (as indicated by (8)), while speed decreases with flux intensity. Hence, self-interested travelers will attempt to utilize all available paved guideways (whose larger capacity allows for faster speed). Meanwhile, an optimized guideway layout should ensure that capacity is provided to the locations of need so that noredundant capacity is provided. As such, the optimized design should reach a spatial "equilibrium" in terms of the "return" on investment in roadway capacity, such that traffic density shall be similar everywhere. The only exception is the area near the sinks where geometry restriction does not

provide sufficient space to build additional capacities even when the traffic density is high.

Similar to Example 1, we cross-check the designs with the parameters. In this example, one of the varying parameters is the maximum pedestrian density $\rho_{\rm max}$, and in general, designs initially optimized for a larger $\rho_{\rm max}$ (or without this constraint) would lead to constraint violations if reevaluating using a smaller $\rho_{\rm max}$. Thus, we exclude the cases with violated constraints. The results of the cross-check are shown in Table 2, with "VIO" denoting violation of maximum pedestrian density constraint. As expected, the lowest objective function appears with the design optimized for the same set of parameters.

Table 2 Cross check of optimized designs and parameters in Fig. 6

Design		Tested parameters									
		$ \rho_{\text{max}} = 0.5 $			$ \rho_{\text{max}} = 1 $			No constraint			
		D = 2.5	D = 5	D = 7.5	D = 2.5	D = 5	D = 7.5	D = 2.5	D = 5	D = 7.5	
$\rho_{\rm max} = 0.5$	D = 2.5	21.19	VIO ^a	VIO	21.19	VIO	VIO	21.19	25.02	29.61	
	D = 5	21.81	24.21	VIO	21.81	24.21	VIO	21.81	24.21	27.86	
	D = 7.5	23.08	25.08	27.80	23.08	25.08	27.80	23.08	25.08	27.80	
$ \rho_{\text{max}} = 1 $	D = 2.5	21.19	VIO	VIO	21.19	VIO	VIO	21.19	25.02	29.61	
	D = 5	21.75	VIO	VIO	21.75	24.14	VIO	21.75	24.14	27.83	
	D = 7.5	22.85	24.76	VIO	22.85	24.76	27.44	22.85	24.76	27.44	
No constraint	D = 2.5	21.19	VIO	VIO	21.19	VIO	VIO	21.19	25.02	29.61	
	D = 5	21.75	VIO	VIO	21.75	24.14	VIO	21.75	24.14	27.83	
	D = 7.5	22.70	VIO	VIO	22.70	24.57	VIO	22.70	24.57	27.22	

a. VIO denotes the density constraint is violated, and hence is not included in the comparison



4.3 Example 3: Quad design

The third example aims at demonstrating the impact of multiplier β on the optimized design. The design domain (150ft × 150ft), boundary conditions (source and sink), and FE mesh are shown in Fig. 8. The FE mesh is 256×256 with 65,536 continuum Q4 elements and 66,049 degrees of freedom (DOFs). A total demand throughput of 15 pedestrians per second is uniformly distributed over three sides (rectangular regions) of the domain, and the sink is located in the middle of the domain with a radius of 75/16 ft. Unit cost and system parameters remain the same as those of the preceding examples. The density filter radius is chosen as $R = 2h_e = 0.585$, and the p-norm in the local traffic density constraint takes the value of $p_n = 12$. The upper and lower bounds on the design variables are $\alpha_0 = 0.2$ (e.g., road capacity of grass with snow) and $\alpha_{\text{max}} = 0.5$ (e.g., road capacity of paved concrete), respectively. The maximum density is set to be $\rho_{\rm max} = 1.0$ (person/sqft).

Figure 9a plots the optimized objective function value over a range of β values, as well as a few pavement designs. Figure 9b shows the final pavement construction cost J_R over the range of β values considered. As β increases (i.e., pavement construction budget decreases), the pavement cost J_R decreases accordingly, and most of the construction concentrates on the area near the sink (where most of the traffic concentrates). Notice that most of the construction is concentrated across the diagonal directions of the square domain, where demand is most clustered. Meanwhile, as β increases, the travel cost J_T also increases but only slowly, probably as a result of reduced pavement construction and worse travel conditions.

If we take a closer look at the guideway design, we can see that for any β , the guideway system is highly aligned with the expected direction of traffic. The major construction concentrates in the southern (lower) half of the area, while some pavements are constructed in the northern

(upper) part—possibly only to help avoid excessive congestion in the south. The "network" of guideway always exhibits some hierarchy structure with curvy "roads." In the south, the thickest guideway is aligned along with 45-degree directions toward the two southern corners (especially for larger values of β ; i.e., under limited construction budget). The thickest guideway in the northern half of the area seems to be along with about 25-degree directions, possibly due to a lack of demand from the northern side.

Figure 10 plots the distributions of pavement construction, equilibrium traffic density, pedestrian cost, as well as the equilibrium flux, for the case with $\beta = 3000$. First, high pedestrian density concentration is observed near the sink, which probably forces guideway construction around the entire perimeter of the sink (so as to allow traffic to enter the sink from all directions). Traffic density in other paved areas is largely constant, as consistent with the observations in Example 2. The traffic paths, as well as the guideways, do not follow straight lines because pedestrians would take detours to avoid overly congested neighborhoods. Near the sink, due to such path-finding behaviors of pedestrians, the equilibrium cost contour ϕ almost form concentric circles. Further away from the sink, the costs become more influenced by the boundary. It is also interesting to notice that, although a greater demand is expected from the south side, construction of the guideway is also more concentrated along with those directions (especially with two 45-degree direct trunks). As a result of such compensation, the travel costs for pedestrians from the northern corners are similar to those from the southern corners. Finally, we take a close look at the flux pattern and compare it with the guideway design. While the majority of traffic stays on paved guideways, we notice that some traffic is carried by unpaved areas (where traffic capacity $\alpha_0 = 0.2 > 0$). Also, we notice how the pedestrian density near guideway boundaries remains continuous, while the flux is locally parallel to the guideway boundary but changes in magnitude, mainly due to change in free-flow speed.

Fig. 8 Example 3. **a** Design domain and boundary conditions; **b** FE mesh using a 256×256 grid

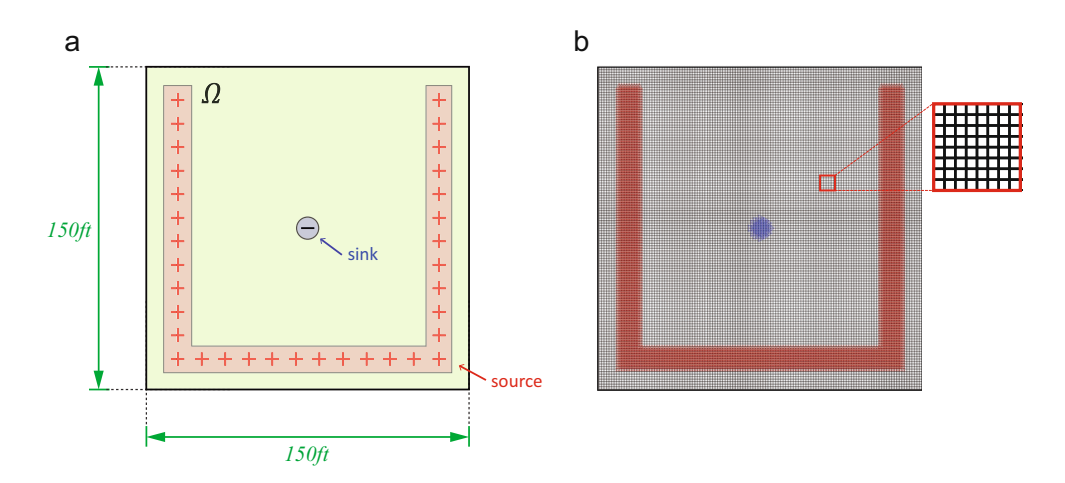




Fig. 9 Example 3: sensitivity of construction budget multiplier β on the optimized results, β takes following values: 0; 500; 1000; 1500; 2000; 2500; 3000; 3500; 4000; 4500; 5000; 6000. a Optimized objective function value (J) and transportation cost (J_T) versus β ; **b** construction cost (J_R) versus β

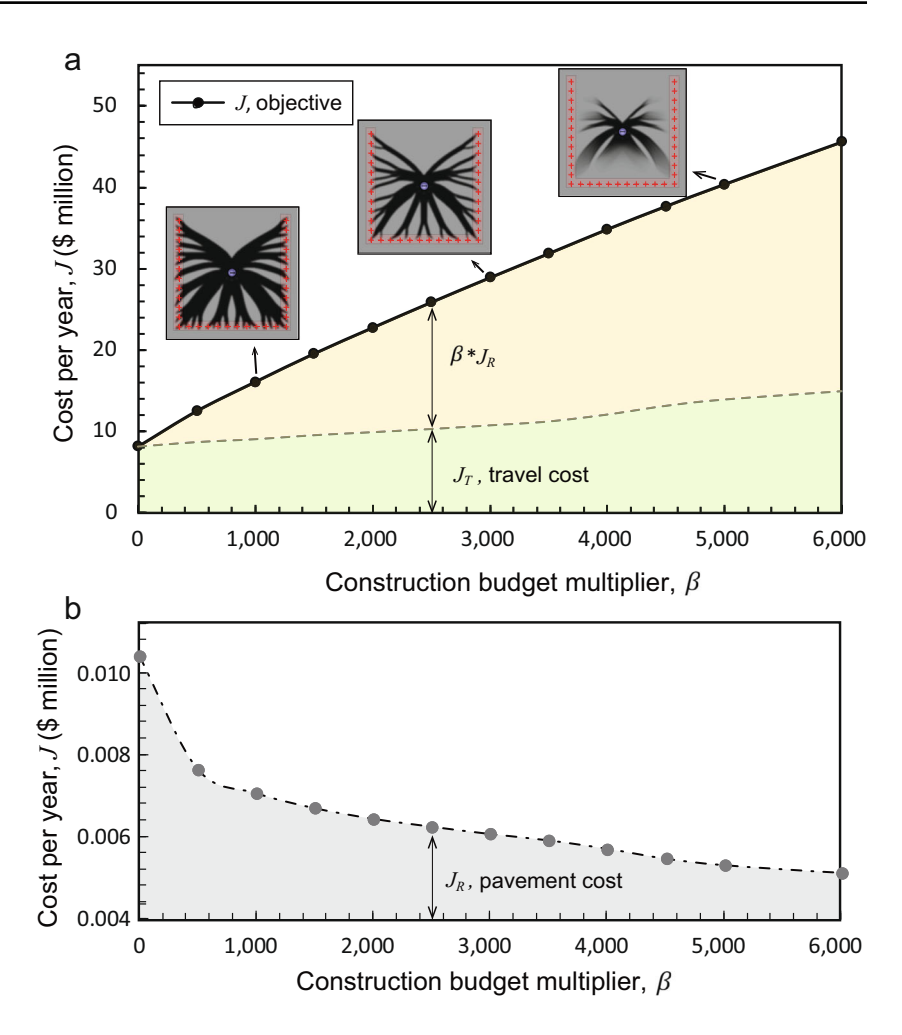


Figure 11 shows both the history of $\max(\rho) - \rho_{\text{max}}$ and objective function convergence over the optimization iterations. We observe that the local pedestrian density constraint is active initially and is then satisfied since optimization iteration 7, which indicates that the pnorm technique to handle local constraints is effective. According to the convergence plot, both the objective function J and transportation cost J_R show some minor oscillations at the first few steps, after which they converge smoothly.

To comprehensively evaluate the optimized design in Fig. 10, we compare it with more conventional or needle-like designs (with straight roads), as in Fig. 12, and optimized needle-like designs, as in Fig. 13. The designs in Fig. 12 use straight roads to connect evenly partitioned source neighborhoods to the sink while using the same amount of pavement construction investment J_R . Their respective objective function values and maximum pedestrian density values are compared with those of the optimized design. As the number of roads increase, the transportation cost drops but the pedestrian concentration worsens. It is shown, nevertheless, that the optimized design

from the proposed model achieves 7% and 2% lower total cost J than the conventional designs and needle-like design, respectively. In terms of transportation cost J_T , the optimized design achieves 18% and 6% lower cost (i.e., achieving efficiency) than the conventional designs and needle-like design, respectively, with a much lower maximum pedestrian density (i.e., ensuring safety).

Figure 13 shows the optimized designs obtained from different initial guesses: the needle-like initial guess, and uniform density initial guess, with two filter radii, and with or without a $\rho_{\rm max}=1$ constraint. The density distribution of the needle-like initial guess is generated using cosine waves along the circular direction with a linear decrease in the radial direction (Yan et al. 2018). As shown in the figures, $\rho_{\rm max}=1$ leads to tree-like structures for both the needle-like and uniform initial guesses, and without using the constraint, needle-like initial guesses lead to lamellar structures with independent paths. In all cases, the designs generated from the uniform initial guess achieve lower objective function values than those from the needle-like initial guesses. Comparing the right-most figures of both rows, we can see the lamellar structures have slightly higher



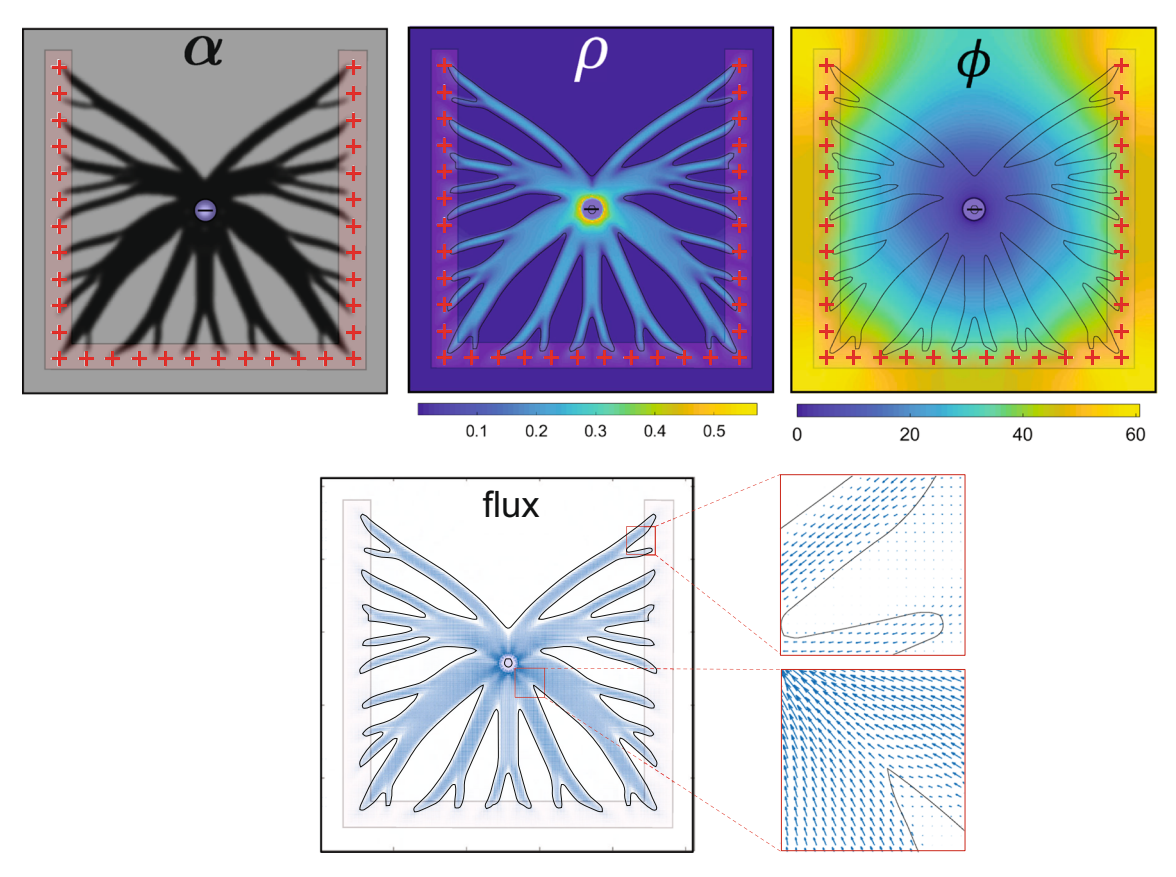
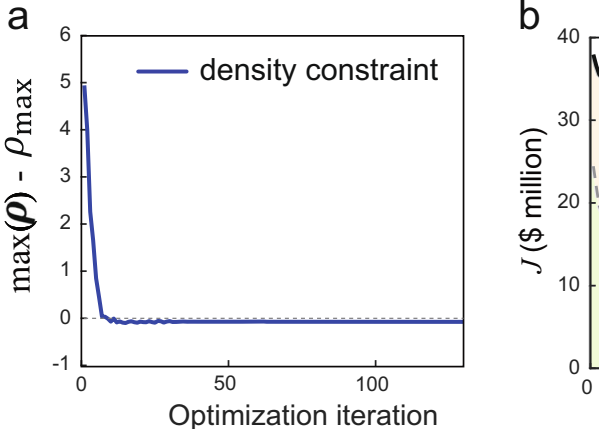
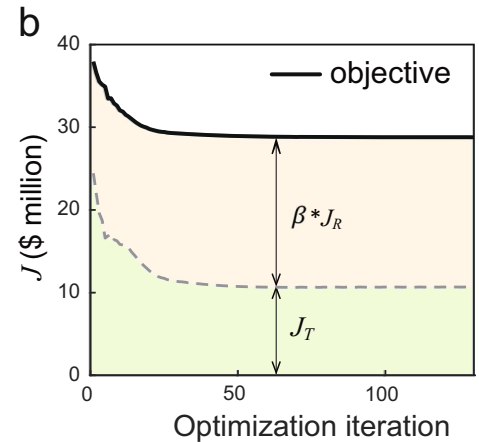


Fig. 10 Example 3: case of $\beta = 3000$. Top left to bottom right: pavement, density, pedestrian cost, and flux distributions

objective function values than the tree-like structures. For linear thermal compliance minimization problems, it has been shown that needle-like structures have lower objective functions than the tree-like structures (Yan et al. 2018). Figure 13 hence shows a different observation, possibly because of the difference in the underlying physical model (based on pedestrian traffic under Nash equilibrium) and objective function.

Fig. 11 Example 3: case of $\beta = 3000$. Local pedestrian density constraint history and objective function convergence history







4.4 Example 4: Tunnel design

This example investigates the impact of traffic boundary conditions on the pavement design, and also demonstrates how adjusting the filter radius effectively control the number of thinner road branches. The design problem is given in Fig. 14, where traffic appears uniformly from the western border and travels to the destinations in the south. We study

Fig. 12 Example 3: Comparison of optimized guideway design and classical guideway designs

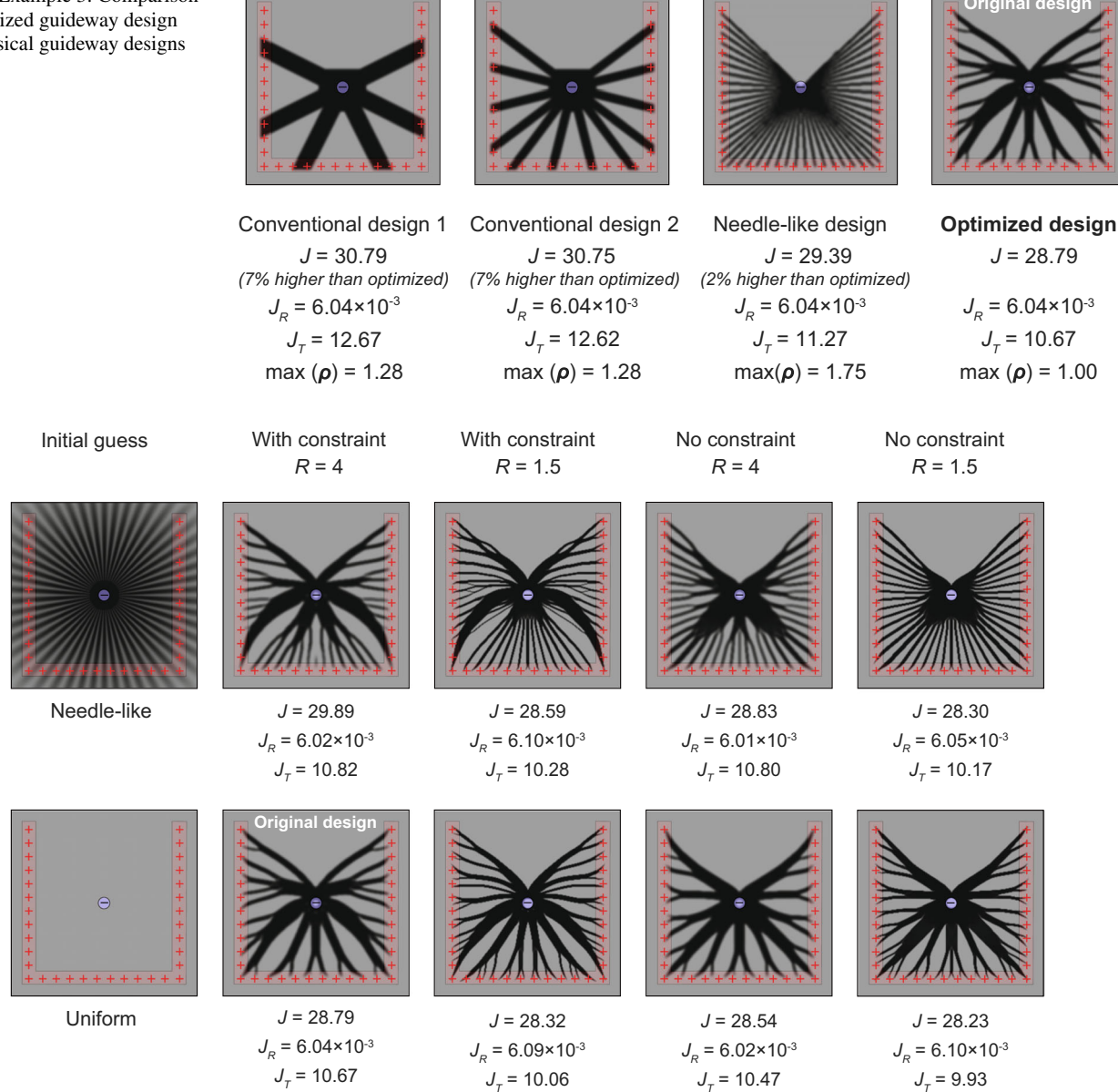


Fig. 13 Example 3: Comparison of optimized designs and needle-like designs

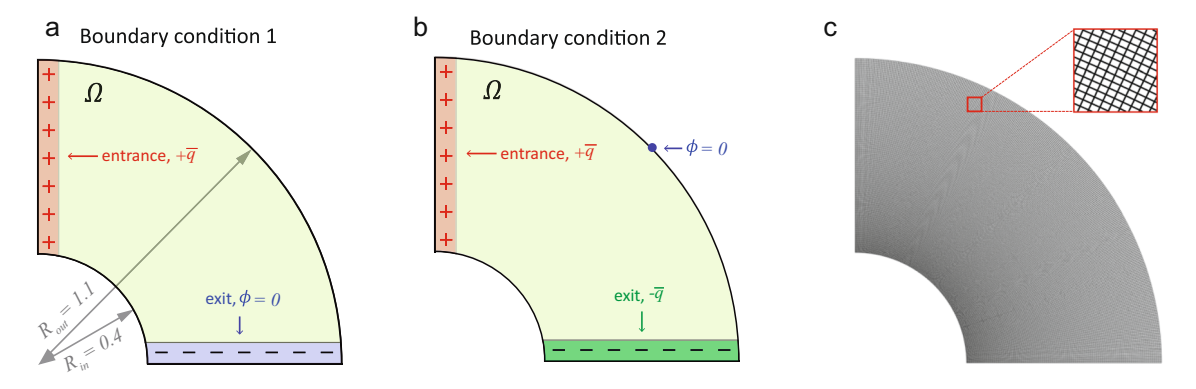


Fig. 14 Example 4. a Design domain and first type of boundary conditions; b design domain and second type of boundary conditions; c finite element mesh using 48,384 elements



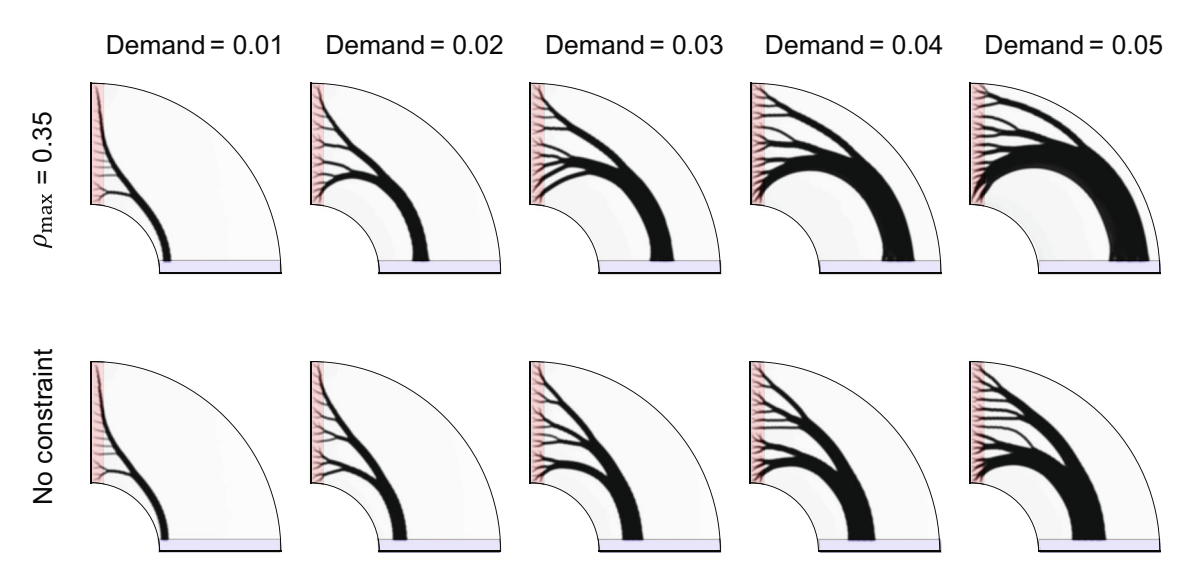


Fig. 15 Example 4: optimized pavement designs with the first boundary condition. First row: with density bound $\rho_{max}=0.35$; second row: without density bound

two types of boundary conditions that represent two distinct outflow traffic scenarios: (1) the southern border of the domain consists of a continuum of exits (each with a width of $1/16 R_{out}$), while all pedestrians are equally willing to go from any of these exits (Fig. 14a); (2) the southern border supports uniformly distributed outflow, whose magnitude is the same as the inflow on the western border (Fig. 14b).

The first boundary condition sets the potential function value $\phi=0$ at all the exits, without explicit control of exit flow distribution across these exits (which is the same setup in all previous examples). The second boundary condition specifies the distribution of traffic outflow but not potential value at the southern exits, so we set the potential function ϕ to be zero only at a single middle point of the outer arc border. The second boundary condition is useful when one aims to achieve a controllable outflow distribution at the exit—possibly due to local capacity considerations. The design domain (with either boundary condition) is discretized into 168 elements in the radial direction and 288 elements in the tangential direction, resulting in a total of 48,384 Q4 elements and 48,841 DOFs. The lower bound on the design variables is $\alpha_0=0.01$ (i.e., near-zero traffic

capacity without pavement construction). The total demand throughput varies from 0.01, 0.02, 0.03, 0.04, to 0.05. The budget constraint multiplier is set to be $\beta = 6000$. Unit costs and other system parameters are the same as those in the preceding examples.

For the first boundary condition, we compare designs of $\rho_{\text{max}} = 0.35$ and $\rho_{\text{max}} = \infty$. The filter radius is set to be $R = 2h_e = 0.0131$, where $h_e = 0.00655$. Figure 15 shows the designs under the first boundary condition. The first row corresponds to $\rho_{\text{max}} = 0.35$, and the second row $\rho_{\text{max}} = \infty$. For all cases, the designs show a tree-like geometry. As the total throughput increases, the roads become thicker as expected, and the shape of the main road changes drastically: from partially curving toward the inner ring to fully curving toward the outer ring. Furthermore, the main road grows in length, possibly due to the increasing dominance of the transportation cost J_T over the construction cost J_C as the throughput rises. In addition, the longer routes in the larger throughput cases have considerably milder changes in the direction and curvature so as to smooth traffic flow. For example, when the demand throughput is 0.05, all branches and the

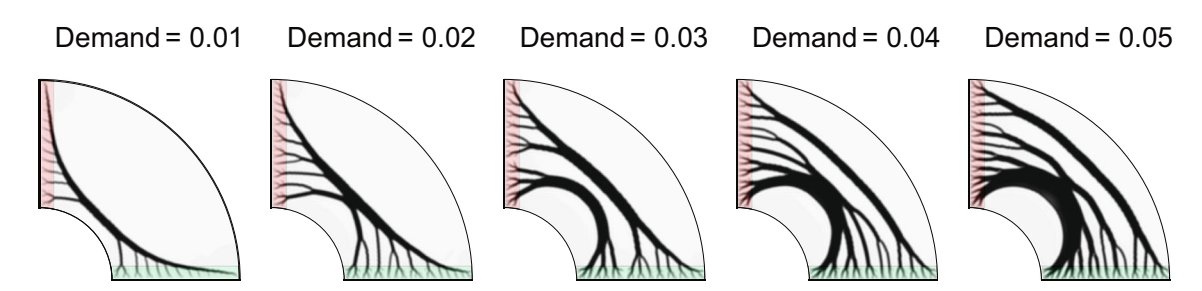
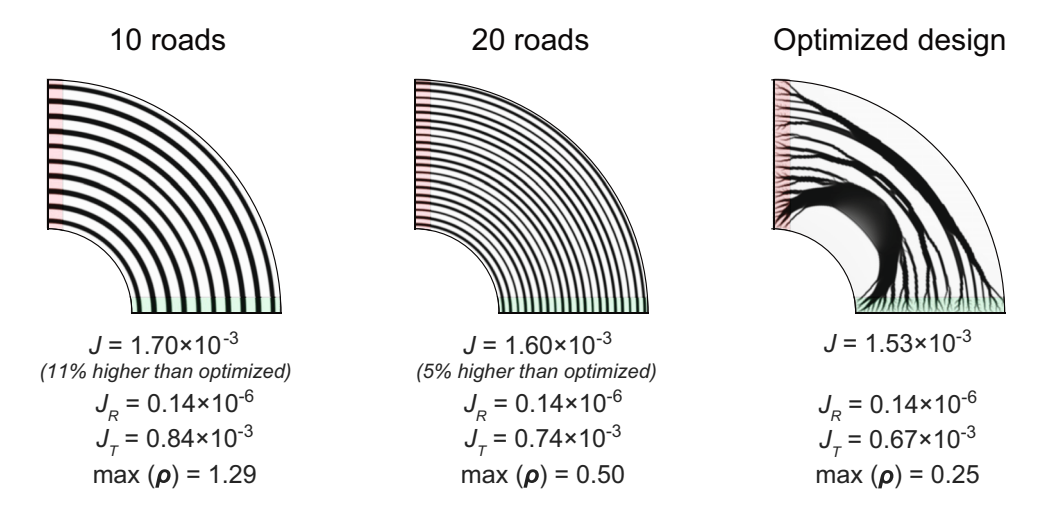


Fig. 16 Example 4: optimized pavement designs with the second boundary condition



Fig. 17 Example 3: Comparison of optimized designs and needle-like designs

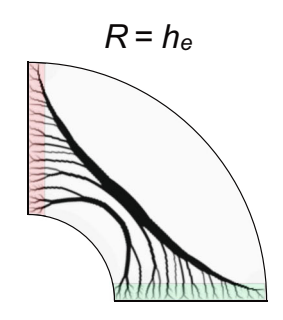


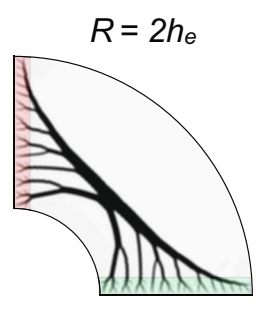
main road curve toward the outer ring; there are no sharp turns. On the contrary, when the demand throughput is 0.01, numerous sharp turns are present where the smaller road branches join the main road.

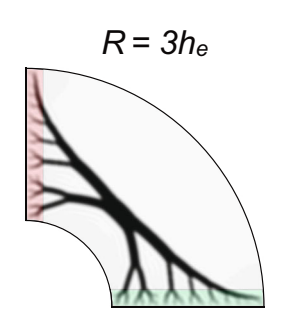
While the shape of the roads and the location of the exit flows have varied considerably under different levels of throughput, the directions of the traffic flow near the sink(s) are identical: perpendicular to the boundary of the sink. This feature is a direct result of the first boundary condition—since $\phi=0$ at all the sinks, its gradient, which is parallel to the local traffic flux, is perpendicular to the $\phi=0$ contour. Comparing the $\rho_{max}=0.35$ case and the $\rho_{max}=\infty$ case, we can see that imposing the maximum density constraint leads to thicker roads and more drastic road shifts mainly near the sinks (where traffic concentrates the most, and density constraints are most likely to be violated).

Figure 16 shows the pavement designs under the second boundary condition where outflow is uniformly distributed along the southern border. The designs are fundamentally different from those under the first boundary condition—there are many small road branches near both the entrance and exit borders. As the total throughput increases, the shape of the main roads bends more toward the outer ring. When the demand throughput ≥ 0.03 , the pavements form separated routes. As the main roads bend outward, the inner branches do not need to bend as much; otherwise, their lengths and construction costs would increase. Finally, the traffic

Fig. 18 Example 4: optimized pavement designs with the second boundary condition using three different filter radius sizes







2 Springer

flux near the exits mostly is not perpendicular to the southern border, mainly because the contours of the potential function are no longer parallel to the border. This feature is in sharp contrast to that under the first boundary condition.

We compare the optimized design of demand = 0.05 to various lamellar designs with many parallel roads in the radial direction, as shown in Fig. 17. The lamellar designs are generated using projected cosine waves and have the same construction costs as the optimized design (right-most design in Fig. 17). All designs in Fig. 17 use a density filter radius $R = h_e$ to preserve the geometric details. The comparison shows that, under the same construction cost, the optimized design obtained from the proposed framework achieves 11% and 5% lower total cost J than the 10-road and 20-road lamellar designs (i.e., due to the lower travel cost), respectively. In addition, the pedestrian densities in all lamellar designs violate the maximum permitted value $\rho_{\text{max}} = 0.25$, whereas the densities in optimized design satisfy the constraint. We conclude that for this problem, the optimized design is not only more efficient but also safer for pedestrians.

Figure 18 shows optimized pavement designs under three density filter radius values, i.e., $R = h_e$, $2h_e$, $3h_e$. The total throughput is 0.02 and the maximum density is $\rho_{\text{max}} = 0.25$. It is observed that changing the filter radius effectively adjusts the width and the number of road branches. A smaller radius results in more but narrower road branches.

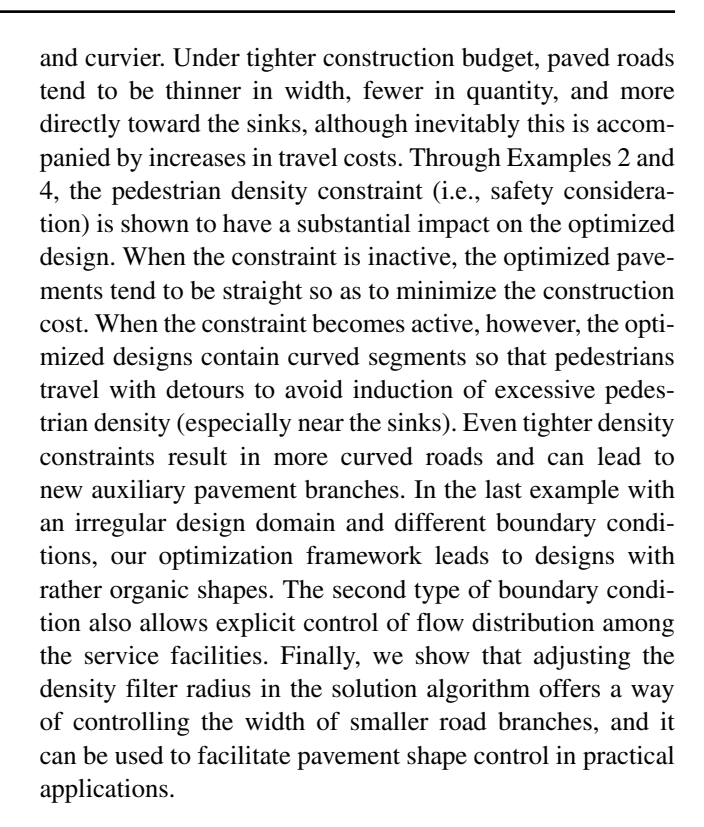
By employing the concept of the filter radius, we can tailor the pavement patterns and offer a control of the local feature of pavement construction.⁵

5 Concluding remarks

In this paper, we present physics-based modeling and optimization frameworks for designing pavement guideway networks that serve congested traffic in a continuous space. The contribution of this study lies in several aspects. First, the optimization framework allows for the design of pavement infrastructures, which alters the road capacity by changing the free-flow travel speed of pedestrians. The objective function minimizes the weighted sum of transportation cost and construction cost. Second, the formulation is built upon a Nash equilibrium model for pedestrian traffic, expressed in the form of a set of nonlinear PDEs. The guideway design influences pedestrians' destination and path choices under congestion. Third, in addition to reducing traffic congestion and guideway construction investment, we also restrict the maximum pedestrian crowd density to ensure public safety. To tackle the overall optimization problem and its state equations, which are highly nonlinear and nonconvex, we present a hybrid solution approach that integrates a fixedpoint iteration method and Newton's method. Last but not the least, we investigate two types of boundary conditions. The first type models zero cost potential at all sinks, while the second type enforces flow distribution at both the sources and sinks.

Through numerical examples, as well as comparison with lamellar structures and more conventional guideway designs, we demonstrate the effectiveness of the proposed physics-based traffic models and topology optimization framework. We investigate the influence of four sets of system parameters, including the total demand throughput, pavement construction budget (multiplier), maximum pedestrian density bound, and traffic boundary conditions. All examples show, as expected, that a higher budget and a higher demand throughput result in more pavement construction, where all road branches become thicker, longer,

⁵The traffic equilibrium model is based on "macroscopic" fluid approximation, where pedestrians are described not as discrete particles but by continuous flux. Hence, the PDE and optimization model do not impose any requirement on the minimum thickness of guideway paths. The congestion delay is dictated by the ratio of flux intensity $|\mathbf{f}|$ to the capacity α , and hence the optimization model tends to provide capacity to the area where flux concentrates. When traffic is dispersed and relatively light (e.g., near the entrances and exits), it is reasonable for the optimization model to yield very thin roads. The density filter is hence needed as a regularization approach to control the length scale to avoid overly thin roads—for practical construction convenience and aesthetic purposes.



Acknowledgments The authors would like to thank Dr. Ole Sigmund for suggesting Example 1. We would also like to acknowledge Dr. K. Svanberg for providing the MMA code.

Funding The work by X. S. Zhang and W. Li were supported in part by the University of Illinois. The work by Y. Ouyang was supported in part by the U.S. National Science Foundation via Grant CMMI-1662825.

Compliance with ethical standards

Conflict of interest On behalf of all authors, the corresponding author states that there is no conflict of interest.

Nomenclature $\alpha(x)$, road capacity at location x; α_0 , minimum road capacity; $\alpha_\ell,$ road capacity of element $\ell;$ $\alpha_{\rm max},$ maximum road capacity; \bar{q} , traffic inflow or outflow at $\partial \Omega$; β , shadow price of construction; α , discretized road capacity vector; λ_{ϱ} , adjoint vector in sensitivity analysis of constraint function g; λ_J , adjoint vector in sensitivity analysis of objective function J; Ω , two-dimensional space; ρ , discretized pedestrian density vector; \tilde{F} , matrix storing the F of previous m AAR iterations; \tilde{R} , matrix storing the R_F of previous m AAR iterations; F, global flux magnitude vector; G_{ℓ} , matrix mapping global degree of freedom vector ${\pmb \Phi}_i$ to $\nabla \phi$ at the center of element $\ell; {\pmb I}$, identity matrix; k_{ℓ}^{0} , element stiffness matrix of element ℓ with $\kappa_{\ell} = 1$; K^{α} , global stiffness matrix; M_{ℓ} , matrix defined by $M_{\ell} := G_{\ell}^{T} G_{\ell}$; n(x), unit normal vector at of $\partial \Omega$; P, density filter matrix; Q, global traffic inflow/outflow vector; R, residual vector in Newton's method; R_F , global residual vector in AAR method; v, vector of element area; x_i , Location of facility i; z, design variable vector; z_{ini} , initial design variable vector; z_{max} , upper bounds of design variable; η , Free flow travel time per unit distance; κ , variable defined as $\kappa := \frac{|\mathbf{f}|}{c}$;



 κ_{ℓ} , κ value associated with element ℓ , assumed to be constant inside element ℓ ; κ_{\min} , a small value to void numerical singularities; **f**, flux vector of pedestrian flows; \mathcal{A}_i , area from where pedestrian travels to facility i; \mathcal{H}_1 , Sobolev space; \mathcal{U} , space of trial functions; \mathcal{U}^0 , space of test functions; \mathcal{U}_h , finite-dimensional trial function space; ϕ , total generalized cost; ϕ_h , finite-dimensional total generalized cost; Φ_i , value of ϕ_h at node i; ψ , test function in weak form; ψ_h , finitedimensional test function; Ψ_i , values of ψ_h at node i; ρ , pedestrian density; ρ_{max} , upper bound for pedestrian density; τ_{opt} , tolerance of change of design variable for terminating optimization; x, position vector; θ , step size in AAR; b_1 , monetary cost to travel a unit distance; b_2 , ratio of capacity to free flow travel speed; c, generalized cost to travel a unit distance; C_R , prorated unit cost for road construction; C_T , monetary value of one unit pedestrian time; E_{ℓ} , area of element ℓ ; $f(\alpha(x))$, prorated cost per unit time for setting a capacity of $\alpha(x)$ for a unit area near x; g, parameter characterizing travel cost sensitivity to congestion; h_e , width of a square quadrilateral element; J, objective function; J_R , total construction cost; J_T , total transportation cost; M, number of nodes in an finite element mesh; N_i , global Lagrange basis function associated with node i; N_{max} , maximum number of optimization steps; p, travel path; p^n , power in p-norm of a ndimensional vector; Pr, period of applying Anderson extrapolation in AAR; q, traffic inflow or outflow in Ω ; R, filter radius; r_0 , radius of facilities; T_h , finite element partition.

Appendix A: A hybrid solution scheme for the nonlinear state equations

To address the challenges described in Section 3.1 associated with solving the nonlinear state equation (29), we propose a robust hybrid solution strategy which combines AAR, a fixed-point iteration method proposed by Suryanarayana et al. (2019) and Banerjee et al. (2016), and the standard Newton's method. In the proposed solution strategy, we first use the AAR to bring the iterate close to the solution and then apply the Newtwon's method to achieve fast convergence.

In the AAR, in order to avoid the difficulty related to the initial guess $\Phi = 0$, we introduce a new global residual vector as

$$\mathbf{R}_{F}(\boldsymbol{\alpha}, \mathbf{F}) = \sum_{\ell}^{n} \kappa_{\ell}(\alpha_{\ell}, |f|_{\ell}) |\nabla_{E_{\ell}} \phi_{h}(\mathbf{F})| - \mathbf{F} = \mathbf{0}, \quad (38)$$

where $|f|_{\ell}$ denotes the flux in element ℓ , $F \in \mathbb{R}^n$ is a vector collecting all the element fluxes, namely, $F = [|f|_1, ..., |f|_n]^T$; and $\kappa(\alpha_{\ell}, |f|_{\ell})$ is defined by relation (13). We note that, unlike the original residual vector $R(\alpha, \Phi)$ defined in (30), where Φ is the independent vector, the new residual vector $R_F(\alpha, F)$ uses the flux vector F as the independent vector and $\Phi(F)$ is obtained from $\Phi = (\mathbf{K}^{\alpha}(\kappa))^{-1} \mathbf{Q}$, where we recall that $\kappa = [\kappa_1, ..., \kappa_n]^T$.

Although defined in different forms and having different independent variables, we can show that $R_F(\alpha, F) = 0$ and $R(\alpha, \Phi) = 0$ are in fact equivalent in the sense that solution of $R_F(\alpha, F) = 0$ is also a solution of $R(\alpha, \Phi) = 0$ and vice versa. The advantage of using $R_F(\alpha, F)$ in the AAR is

that it allows us to use a non-zero initial guess for vector F which, according to Fig. 1, will can lead to well-conditioned matrix \mathbf{K}^{α} . In our implementation, we use F = 1 as the initial guess for AAR in the first optimization step and, in the subsequent optimization steps, F is initialized using the converged F from the previous optimization step. This choice has been shown to be effective and robust for all the numerical examples in this work.

The AAR iteration to update the flux vector \mathbf{F} as:

$$\mathbf{F}^{(k+1)} = \max\left(\mathbf{F}^{(k)} + \mathbf{B}^{(k)}\mathbf{R}_F(\boldsymbol{\alpha}, \mathbf{F}^{(k)}), \mathbf{0}\right), \tag{39}$$

where $F^{(k)}$ is the flux vector at the kth AAR iteration, $\max(\cdot, \cdot)$ stands for the element-wise maximum operator between the two vectors, and the matrix $\mathbf{B}^{(k)}$ is defined by:

$$\mathbf{B}^{(k)} = \begin{cases} \theta \mathbf{I} & \text{if } (k+1)/Pr \notin \mathbb{N} \\ \theta \mathbf{I} - (\tilde{\mathbf{F}}^{(k)} + \theta \tilde{\mathbf{R}}^{(k)}) (\tilde{\mathbf{R}}^{(k),T} \tilde{\mathbf{R}}^{(k)})^{-1} \tilde{\mathbf{R}}^{(k),T} & \text{if } (k+1)/Pr \in \mathbb{N} \end{cases}$$
(40)

where θ is the step size, Pr is the period of applying Anderson mixing (Anderson 1965), and $\tilde{\mathbf{F}}^{(k)} \in \mathbb{R}^{n \times m}$ and $\tilde{\mathbf{R}}^{(k)} \in \mathbb{R}^{n \times m}$ are matrices collecting history information of flux and residual vectors:

$$\tilde{\mathbf{F}}^{(k)} = \left[\Delta \mathbf{F}^{(k-m)} \ \Delta \mathbf{F}^{(k-m+1)} \ \dots \ \Delta \mathbf{F}^{(k-1)} \right]$$
(41)

$$\tilde{\mathbf{R}}^{(k)} = \left[\Delta \mathbf{R}_F(\boldsymbol{\alpha}, \mathbf{F}^{(k-m)}) \ \Delta \mathbf{R}_F(\boldsymbol{\alpha}, \mathbf{F}^{(k-m+1)}) \ \dots \ \Delta \mathbf{R}_F(\boldsymbol{\alpha}, \mathbf{F}^{(k-1)}) \right],$$
(42)

and $\Delta F^{(j)} = F^{(j+1)} - F^{(j)}$, $\Delta R_F(\alpha, F^{(j)}) = R_F(\alpha, F^{(j+1)}) - R_F(\alpha, F^{(j)})$. We note that, by defining matrix **B** using (40), we essentially apply a quasi-Newton Anderson mixing (Anderson 1965) every Pr iterations. In other iterations, the simple Richardson iteration is used. For all the examples in this work, we use $\theta = 0.5$, m = 5, and $R_r = 4$. The AAR iteration is terminated when the ℓ_2 -norm of the residual vector $\mathbf{R}_F(\alpha, F)$ is below 10^{-3} . The corresponding $\boldsymbol{\Phi} = (\mathbf{K}^{\alpha}(\kappa))^{-1} \boldsymbol{Q}$ is then taken as the initial guess of the Newton's method described below.

In the Newton's method, we will switch back to the original residual vector \mathbf{R} in (30). At iteration k of the Newton's method, we linearize the above nonlinear system of equations as

$$R(\alpha, \Phi) \approx R(\alpha, \Phi^{(k)}) + K_T^{\alpha} \left(\kappa(\alpha, \Phi^{(k)}) \right) \Delta \Phi^{(k)} = 0, (43)$$

where $\mathbf{K}_T^{\alpha} \doteq \partial \mathbf{R}/\partial \mathbf{\Phi}$ is the tangent stiffness matrix. Solving the linearized system gives

$$\Delta \boldsymbol{\Phi}^{(k)} = \left[\mathbf{K}_T^{\alpha} \left(\kappa(\boldsymbol{\alpha}, \boldsymbol{\Phi}^{(k)}) \right) \right]^{-1} \boldsymbol{R}(\boldsymbol{\Phi}^k), \tag{44}$$

which leads to the recurrent update formula $\Phi^{k+1} = \Phi^k + \Delta \Phi^k$ until the ℓ_2 -norm of the residual vector is below tolerance 10^{-5} .



A consistently linearized tangent stiffness matrix is essential to ensure the convergence of the Newton's method. Thus, in the remainder of this appendix, a detailed derivation of the consistent tangent stiffness matrix \mathbf{K}_T^{α} is provided.

By definition and using the chain rule, we have

$$\mathbf{K}_{T}^{\alpha}\left(\kappa(\boldsymbol{\alpha},\boldsymbol{\Phi})\right) = \frac{\partial \boldsymbol{R}}{\partial \boldsymbol{\Phi}}(\boldsymbol{\alpha},\boldsymbol{\Phi})$$
$$= \frac{\partial \mathbf{K}^{\alpha}}{\partial \boldsymbol{\Phi}}\left(\kappa(\boldsymbol{\alpha},\boldsymbol{\Phi})\right)\boldsymbol{\Phi} + \mathbf{K}^{\alpha}\left(\kappa(\boldsymbol{\alpha},\boldsymbol{\Phi})\right) \tag{45}$$

To obtain an explicit expression of \mathbf{K}_T^{α} , we first compute the following local matrix as

$$[\mathbf{k}_{\ell}^{\boldsymbol{\Phi}}]_{ij} = \frac{\partial \kappa_{\ell}}{\partial \boldsymbol{\Phi}_{j}} \left(\sum_{m} [\mathbf{k}_{\ell}^{0}]_{im} \boldsymbol{\Phi}_{m} \right), \tag{46}$$

where the derivative $\partial \kappa_{\ell}/\partial \Phi_{j}$ can be computed as follows

$$\frac{\partial \kappa_{\ell}}{\partial \boldsymbol{\Phi}_{j}} = \frac{\partial \kappa_{\ell}}{\partial |\nabla_{E_{\ell}} \boldsymbol{\phi}_{h}|} \frac{\partial |\nabla_{E_{\ell}} \boldsymbol{\phi}_{h}|}{\partial \boldsymbol{\Phi}_{j}} = \frac{\partial \kappa_{\ell}}{\partial |\nabla_{E_{\ell}} \boldsymbol{\phi}_{h}|} \frac{\sum_{i} [\mathbf{M}_{\ell}]_{ji} \boldsymbol{\Phi}_{i}}{2\sqrt{\boldsymbol{\Phi}^{T} \mathbf{M}_{\ell} \boldsymbol{\Phi}}}$$

$$(47)$$

Since κ_{ℓ} is defined implicitly through $h(\kappa_{\ell}, \alpha_{\ell}, |\nabla_{E_{\ell}}\phi_{h}|) = 0$, see (15) and Footnote 4, we can compute the derivative $\partial \kappa_{\ell}/\partial |\nabla_{E_{\ell}}\phi_{h}|$ as

$$\frac{dh}{d|\nabla_{E_{\ell}}\phi_{h}|} = \frac{\partial h(\kappa_{\ell}, \alpha_{\ell}, |\nabla_{E_{\ell}}\phi_{h}|)}{\partial \kappa_{\ell}} \frac{\partial \kappa_{\ell}}{\partial |\nabla_{E_{\ell}}\phi_{h}|} + \frac{\partial h(\kappa_{\ell}, \alpha_{\ell}, |\nabla_{E_{\ell}}\phi_{h}|)}{\partial |\nabla_{E_{\ell}}\phi_{h}|} = 0,$$
(48)

which gives

$$\frac{\partial \kappa_{\ell}}{\partial |\nabla_{E_{\ell}} \phi_{h}|} = -\frac{\partial h(\kappa_{\ell}, \alpha_{\ell}, |\nabla_{E_{\ell}} \phi_{h}|) / \partial |\nabla_{E_{\ell}} \phi_{h}|}{\partial h(\kappa_{\ell}, \alpha_{\ell}, |\nabla_{E_{\ell}} \phi_{h}|) / \partial \kappa_{\ell}}$$
(49)

Finally, the global tangent stiffness matrix can be given by

$$\mathbf{K}_{T}^{\alpha}(\boldsymbol{\alpha}, \boldsymbol{\Phi}) = \sum_{\ell=1}^{M} \left(\mathbf{k}_{\ell}^{\boldsymbol{\Phi}} + \kappa_{\ell}(\alpha_{\ell}, |\nabla_{E_{\ell}} \phi_{h}|) \mathbf{k}_{\ell}^{0} \right)$$
 (50)

Appendix B: Sensitivity analysis

The sensitivities of the objective function J and constraint function g with respect to the design variable z_{ℓ} can be obtained from the adjoint method as

$$\frac{\partial J}{\partial z_{\ell}} = \sum_{i=1}^{n} \left[\frac{\partial J(\boldsymbol{\alpha}, \boldsymbol{\rho})}{\partial \alpha_{m}} + \frac{\partial J(\boldsymbol{\alpha}, \boldsymbol{\rho})}{\partial \rho_{m}} \frac{\partial \rho_{m}}{\partial \alpha_{m}} + \lambda_{J}^{T} \frac{\partial R(\boldsymbol{\alpha}, \boldsymbol{\Phi})}{\partial \alpha_{m}} \right] \frac{\partial \alpha_{m}}{\partial z_{\ell}} \quad \text{and (51)}$$

$$\frac{\partial g}{\partial z_{\ell}} = \sum_{m=1}^{n} \left[\frac{\partial g(\boldsymbol{\rho})}{\partial \rho_{m}} \frac{\partial \rho_{m}}{\partial \alpha_{m}} + \boldsymbol{\lambda}_{g}^{T} \frac{\partial \boldsymbol{R}(\boldsymbol{\alpha}, \boldsymbol{\Phi})}{\partial \alpha_{m}} \right] \frac{\partial \alpha_{m}}{\partial z_{\ell}}$$
(52)

respectively, where λ_J and λ_g are the vectors of adjoint variables given by

$$\lambda_{J} = -\left(\mathbf{K}_{T}^{\alpha}(\boldsymbol{\alpha}, \boldsymbol{\Phi})\right)^{-T} \left(\sum_{m=1}^{n} \frac{\partial J(\boldsymbol{\alpha}, \boldsymbol{\rho})}{\partial \rho_{m}} \frac{\partial \rho_{m}}{\partial \boldsymbol{\Phi}}\right) \quad \text{and (53)}$$

$$\lambda_{g} = -\left(\mathbf{K}_{T}^{\alpha}(\boldsymbol{\alpha}, \boldsymbol{\Phi})\right)^{-T} \left(\sum_{m=1}^{n} \frac{\partial g(\boldsymbol{\rho})}{\partial \rho_{m}} \frac{\partial \rho_{m}}{\partial \boldsymbol{\Phi}}\right)$$
(54)

respectively, with \mathbf{K}_T^{α} being evaluated at the converged solution of each optimization step and black $\partial \alpha_m/\partial z_\ell = [\mathbf{P}]_{m\ell}$.

In the above expressions for sensitivity analysis, the detailed expressions of $\partial J/\partial \alpha_m$, $\partial J/\partial \rho_m$, $\partial g/\partial \rho_m$ and $\partial R/\partial \alpha_m$ are given below:

$$\frac{\partial J(\boldsymbol{\alpha}, \boldsymbol{\rho})}{\partial \alpha_m} = \beta \, C_B \, v_m; \qquad \frac{\partial J(\boldsymbol{\alpha}, \boldsymbol{\rho})}{\partial \rho_m} = (1 - \beta) \, C_T v_m; \quad (55)$$

$$\frac{\partial g(\boldsymbol{\rho})}{\partial \rho_m} = \left(\sum_{j=1}^n \left(\rho_j\right)^{p_n}\right)^{\frac{1}{p_n}-1} \left(\rho_m\right)^{p_n-1};\tag{56}$$

$$\frac{\partial \mathbf{R}(\alpha, \mathbf{\Phi})}{\partial \alpha_m} = \frac{\partial \mathbf{K}^{\alpha}(\alpha, \mathbf{\Phi})}{\partial \alpha_m} \mathbf{\Phi} = \frac{\partial \kappa_m}{\partial \alpha_m} \mathbf{k}_m^0 \mathbf{\Phi}$$
 (57)

Additionally, the detailed expressions of $\partial \kappa_m/\partial \alpha_m$ in the above expressions can be obtained in the similar manner as $\partial \kappa_m/\partial |\nabla_{E_m}\phi_h|$ (i.e., (48)–(49)) as

$$\frac{\partial \kappa_m}{\partial \alpha_m} = -\frac{\partial h(\kappa_m, \alpha_m, |\nabla_{E_m} \phi_h|)/\partial \alpha_m}{\partial h(\kappa_m, \alpha_m, |\nabla_{E_m} \phi_h|)/\partial \kappa_m},\tag{58}$$

with κ_m and $|\nabla_{E_m}\phi_h|$ being evaluated at the converged solution of each optimization step. Once $\partial \kappa_m/\partial \alpha_m$ is obtained, we can further compute $\partial \rho_m/\partial \alpha_m$ and $\partial \rho_m/\partial \Phi$ based on (34) as

$$\frac{\partial \rho_{m}(\alpha_{m}, \boldsymbol{\Phi})}{\partial \alpha_{m}} = \frac{\partial \rho_{m}}{\partial \alpha_{m}} + \frac{\partial \rho_{m}}{\partial \kappa_{m}} \frac{\partial \kappa_{m}}{\partial \alpha_{m}}$$

$$= -|\nabla_{E_{m}} \phi_{h}| \frac{\kappa_{m}}{\alpha_{m}} \left[\frac{b_{2}}{\alpha_{m}} + g \left(\frac{\kappa_{m} |\nabla_{E_{m}} \phi_{h}|}{\alpha_{m}^{g+1}} \right)^{g} \right]$$

$$+ |\nabla_{E_{m}} \phi_{h}| \left[\frac{b_{2}}{\alpha_{m}} + (g+1) \left(\frac{\kappa_{m} |\nabla_{E_{m}} \phi_{h}|}{\alpha_{m}} \right)^{g} \right] \frac{\partial \kappa_{m}}{\partial \alpha_{m}} \tag{59}$$

and

$$\frac{\partial \rho_{m}(\alpha_{m}, \boldsymbol{\Phi})}{\partial \boldsymbol{\Phi}} = \left[\frac{\partial \rho_{m}}{\partial |\nabla_{E_{m}} \phi_{h}|} + \frac{\partial \rho_{m}}{\partial \kappa_{m}} \frac{\partial \kappa_{m}}{\partial |\nabla_{E_{m}} \phi_{h}|} \right] \frac{\partial |\nabla_{E_{m}} \phi_{h}|}{\partial \boldsymbol{\Phi}}$$

$$= \left(\kappa_{m} + |\nabla_{E_{m}} \phi_{h}| \frac{\partial \kappa_{m}}{\partial |\nabla_{E_{m}} \phi_{h}|} \right)$$

$$\times \left[\frac{b_{2}}{\alpha_{m}} + (g+1) \left(\frac{\kappa_{m} |\nabla_{E_{m}} \phi_{h}|}{\alpha_{m}} \right)^{g} \right] \frac{\mathbf{M}_{m} \boldsymbol{\Phi}}{\sqrt{\boldsymbol{\Phi}^{T} \mathbf{M}_{m} \boldsymbol{\Phi}}}, (60)$$

where both $\partial \kappa/\partial \alpha_m$ and $\partial \kappa/\partial |\nabla_{E_m} \phi_h|$ are obtained by evaluating (58) and (49) at the converged solution of each optimization step.



Replication of results Data are available from authors upon request.

References

- Aage N, Andreassen E, Lazarov BS, Sigmund O (2017) Giga-voxel computational morphogenesis for structural design. Nature 550:84
- Alexandersen J, Andreasen C (2020) A review of topology optimisation for fluid-based problems. Fluids 5(29)
- Alexandersen J, Sigmund O, Aage N (2016) Large scale threedimensional topology optimisation of heat sinks cooled by natural convection. Int J Heat Mass Transfer 100:876–891
- An S, Cui N, Bai Y, Xie W, Chen M, Ouyang Y (2015) Reliable emergency service facility location under facility disruption, en-route congestion and in-facility queuing. Transp Res E 82:199–216
- Anderson DG (1965) Iterative procedures for nonlinear integral equations. J ACM (JACM) 12(4):547–560
- Bai Y, Hwang T, Kang S, Ouyang Y (2011) Biofuel refinery location and supply chain planning under traffic congestion. Trans Res Part B Meth 45(1):162–175
- Bai Y, Ouyang Y, Pang J (2016) Enhanced models and improved solution for competitive biofuel supply chain design under land use constraints. Eur J Oper Res 249(1):281–297
- Banerjee AS, Suryanarayana P, Pask JE (2016) Periodic pulay method for robust and efficient convergence acceleration of self-consistent field iterations. Chem Phys Lett 647:31–35
- BBC News (2015) Shanghai new year crush kills 36. Web link: https://www.bbc.com/news/world-asia-china-30646918
- Beghini LL, Beghini A, Katz N, Baker WF, Paulino GH (2014) Connecting architecture and engineering through structural topology optimization. Eng Struct 59:716–726
- Bendsøe MP, Kikuchi N (1988) Generating optimal topologies in structural design using a homogenization method. Comput Meth Appl Mechan Eng 71(2):197–224. https://doi.org/10.1016/0045-7825(88)90086-2. http://www.sciencedirect.com/science/article/pii/0045782588900862
- Bendsøe MP, Sigmund O (2003) Topology optimization: theory, methods, and applications. Springer, Berlin
- Borrvall T, Petersson J (2003) Topology optimization of fluids in stokes flow. Int J Numer Methods Fluids 41(1):77–107
- Bourdin B (2001) Filters in topology optimization. Int J Numer Methods Eng 50(9):2143–2158
- Christiansen RE, Wang F, Sigmund O (2019) Designing photonic topological insulators with quantum-spin-hall edge states using topology optimization. Nanophotonics 8:1363–1369
- Clausen A, Wang F, Jensen JS, Sigmund O, Lewis JA (2015) Topology optimized architectures with programmable poisson's ratio over large deformations. Adv Mater 27(37):5523–5527
- Da D, Yvonnet J, Xia L, Li G (2018) Topology optimization of particle-matrix composites for optimal fracture resistance taking into account interfacial damage. Int J Numer Methods Eng 115(5):604–626
- Deaton JD, Grandhi RV (2014) A survey of structural and multidisciplinary continuum topology optimization: post 2000. Struct Multidiscip Optim 49(1):1–38. https://doi.org/10.1007/s00158-013-0956-z
- Duysinx P, Sigmund O (1998) New developments in handling stress constraints in optimal material distribution, 7th AIAA/USAF/NASA/ISSMO Symposium on Multidisciplinary Analysis and Optimization, American Institute of Aeronautics and Astronautics, 0. https://doi.org/10.2514/6.1998-4906
- Gersborg-Hansen A, Bendsøe MP, Sigmund O (2006) Topology optimization of heat conduction problems using the

- finite volume method. Struct Multidiscip Optim 31(4):251–259. https://doi.org/10.1007/s00158-005-0584-3
- Gladstone R (2015) Death toll from hajj stampede reaches 2,411 in new estimate
- Guenther R, Lee J (1996) Partial differential equations of mathematical physics and integral equations. Dover books on mathematics, Dover Publications
- Hajibabai L, Ouyang Y (2013) Integrated planning of supply chain networks and multimodal transportation infrastructure expansion: model development and application to the biofuel industry. Comput-Aided Civ Inf Eng 28(4):247–259
- Hajibabai L, Bai Y, Ouyang Y (2014) Joint optimization of freight facility location and pavement infrastructure rehabilitation under network traffic equilibrium. Trans Res Part B Meth 63:38–52
- Helbing D (1991) A mathematical model for the behavior of pedestrians. Behav Sci 36(4):298–310
- Helbing D, Molnar P (1995) Social force model for pedestrian dynamics. Phys Rev E 51(5):4282
- Helbing D, Buzna L, Johansson A, Werner T (2005) Self-organized pedestrian crowd dynamics: experiments, simulations, and design solutions. Trans Sci 39(1):1–24
- Helbing Dirk JK, Molnar P (1997) Modelling the evolution of human trail systems. Nature 388:47–50
- Hoogendoorn S, Campanella M, Daamen W (2011) Fundamental Diagrams for Pedestrian Networks. In: Peacock R, Kuligowski E, Averill J (eds) Pedestrian and Evacuation Dynamics. Springer, Boston, MA, pp 255–264
- Jiang L, Li J, Shen C, Yang S, Han Z (2014) Obstacle optimization for panic flow-reducing the tangential momentum increases the escape speed. PloS one 9(12) e115:463
- Johansson A, Helbing D (2007) Pedestrian flow optimization with a genetic algorithm based on boolean grids. Springer, pp 267–272
- Konur D, Geunes J (2011) Analysis of traffic congestion costs in a competitive supply chain. Trans Res Part E Logist Trans Rev 47(1):1–17
- Konur D, Geunes J (2012) Competitive multi-facility location games with non-identical firms and convex traffic congestion costs. Trans Res Part E Logist Trans Rev 48(1):373–385
- Li AC, Nozick L, Xu N, Davidson R (2012) Shelter location and transportation planning under hurricane conditions. Trans Res Part E Logist Trans Rev 48(4):715–729
- Little JDC (1961) A proof for the queuing formula: L = w. Oper Res 9:296–435
- Maute K, Allen M (2004) Conceptual design of aeroelastic structures by topology optimization. Struct Multidiscip Optim 27(1):27–42. https://doi.org/10.1007/s00158-003-0362-z
- Ouyang Y, Wang Z, Yang H (2015) Facility location design under continuous traffic equilibrium. Transp Res Part B 81(1):18–33
- Russ JB, Waisman H (2020) A novel topology optimization formulation for enhancing fracture resistance with a single quasi-brittle material. Int J Numer Methods Eng 121(13):2827–2856
- Ryu JC, Park FC, Kim YY (2012) Mobile robot path planning algorithm by equivalent conduction heat flow topology optimization. Struct Multidiscip Optim 45(5):703–715
- Sherali HD, Carter TB, Hobeika AG (1991) A location-allocation model and algorithm for evacuation planning under hurricane/flood conditions. Trans Res Part B Meth 25(6):439–452
- Sigmund O (1994) Materials with prescribed constitutive parameters: an inverse homogenization problem. Int J Solids Struct 31(17):2313–2329
- Sigmund O (1995) Tailoring materials with prescribed elastic properties. Mech Mater 20(4):351–368
- Sigmund O, Maute K (2013) Topology optimization approaches. Struct Multidiscip Optim 48(6):1031–1055. https://doi.org/10. 1007/s00158-013-0978-6



- Suryanarayana P, Pratapa PP, Pask JE (2019) Alternating andersonrichardson method: an efficient alternative to preconditioned krylov methods for large, sparse linear systems. Comput Phys Commun 234:278–285
- Svanberg K (1987) The method of moving asymptotes a new method for structural optimization. Int J Numer Methods Eng 24(2):359–373
- Wadbro E, Noreland D (2019) Continuous transportation as a material distribution topology optimization problem. Struct Multidiscip Optim 59(5):1471–1482
- Wang F, Sigmund O, Jensen JS (2014) Design of materials with prescribed nonlinear properties. Journal of the Mechanics and Physics of Solids 69:156–174
- Wang F, Christiansen RE, Yu Y, M
 ørk J, Sigmund O (2018) Maximizing the quality factor to mode volume ratio for ultra-small photonic crystal cavities. Appl Phys Lett 113(24):241, 101
- Wang Z (2017) Planning Service Facilities and Infrastructures Under Continuous Traffic Equilibrium. PhD Dissertation. University of Illinois at Urbana-Champaign
- Wang Z, Ouyang Y (2016) On solving a class of continuous traffic equilibrium problems and planning facility location under congestion. Revision Under Review
- Wang Z, Xie S, Ouyang Y (2019) Planning facility location in a continuous space under congestion and disruption risks. Under Revision
- Wardrop J. (1952) Some Theoretical Aspects of Road Traffic Research. ICE Proceedings: Engineering Divisions. pp. 325–362.
- Xia L, Breitkopf P (2015) Design of materials using topology optimization and energy-based homogenization approach in matlab. Struct Multidiscip Optim 52(6):1229–1241. https://doi.org/10.1007/s00158-015-1294-0

- Yan S, Wang F, Sigmund O (2018) On the non-optimality of tree structures for heat conduction. Int J Heat Mass Trans 122:660–680. https://doi.org/10.1016/j.ijheatmasstransfer.2018.01.114. http://www.sciencedirect.com/science/article/pii/S0017931017351566
- Yang H (1996) A spatial price equilibrium model with congestion effects. Ann Reg Sci 30(4):359–371
- Yang H, Wong S (2000) A continuous equilibrium model for estimating market areas of competitive facilities with elastic demand and market externality. Transp Sci 34(2):216–227
- Yang H, Yagar S, Iida Y (1994) Traffic assignment in a congested discrete/continuous transportation system. Trans Res Part B Meth 28(2):161–174
- Zhang X, Ramos AS Jr, Paulino GH (2017) Material nonlinear topology design using the ground structure method with a discrete filter scheme. Struct Multidiscip Optim 55(6):2045–2072
- Zhang XS, de Sturler E, Paulino GH (2017) Stochastic sampling for deterministic structural topology optimization with many load cases: Density-based and ground structure approaches. Comput Methods Appl Mech Eng 325:463–487
- Zhang XS, Paulino GH, Ramos AS Jr (2018) Multi-material topology optimization with multiple volume constraints: a ground structure approach involving material nonlinearity. Struct Multidiscip Optim 57:161–182
- Zhu JH, Zhang WH, Xia L (2016) Topology optimization in aircraft and aerospace structures design. Arch Comput Methods Eng 23(4):595–622. https://doi.org/10.1007/s11831-015-9151-2

Publisher's note Springer Nature remains neutral with regard to jurisdictional claims in published maps and institutional affiliations.

